2010
2011

GENEESKUNDE

master in de biomedische wetenschappen: bio-elektronica en nanotechnologie

Masterproef

Nanocrystalline Diamond Coating of Cardiac Stimulation Electrodes For Improved Biocompatibility: A Structural And Electrochemical Investigation

Promotor :
Prof. dr. Milos NESLADEK
Prof. dr. Patrick WAGNER

Romano Rendace

Masterproef voorgedragen tot het bekomen van de graad van master in de biomedische wetenschappen , afstudeerrichting bio-elektronica en nanotechnologie

Maastricht University

universiteit hasselt
UNIVERSITEIT VAN DE TOEKOMST

De transnationale Universiteit Limburg is een uniek samenwerkingsverband van twee universiteiten in twee landen: de Universiteit Hasselt en Maastricht University

universiteit hasselt
UNIVERSITEIT VAN DE TOEKOMST

Maastricht University

Universiteit Hasselt | Campus Diepenbeek | Agoralaan Gebouw D | BE-3590 Diepenbeek
Universiteit Hasselt | Campus Hasselt | Martelarenlaan 42 | BE-3500 Hasselt

2010
2011

GENEESKUNDE

master in de biomedische wetenschappen: bio-elektronica en nanotechnologie

Masterproef

Nanocrystalline Diamond Coating of Cardiac Stimulation Electrodes For Improved Biocompatibility: A Structural And Electrochemical Investigation

Promotor :
Prof. dr. Milos NESLADEK
Prof. dr. Patrick WAGNER

Romano Rendace

Masterproef voorgedragen tot het bekomen van de graad van master in de biomedische wetenschappen , afstudeerrichting bio-elektronica en nanotechnologie

Maastricht University

universiteit hasselt
UNIVERSITEIT VAN DE TOEKOMST

Table of Contents

Abbreviations

ICD = Implantable Cardioverter-Defibrillator

FBR = foreign body reaction

MWPECVD = microwave plasma enhanced chemical vapor deposition

CVD = chemical vapor deposition

UNCD = ultrananocrystalline diamond

NCD = nanocrystalline diamond

nm = nanometer

SEM = scanning electron microscopy

AFM = atomic force microscopy

EIS = electrochemical impedance spectroscopy

CV = cyclic voltammetry

Ti = titanium

Ir = iridium

Pl/Ir = platinum/iridium

SS = stainless steel

cm = centimeter

mg/l = milligram/liter

CDA = clean dry air

HF = high frequency

°C = degrees Celsius

mBar= millibar

H = hydrogen

CH_4 = methane

CO_2 = carbon dioxide

kW = kilowatt

kHz= kilohertz

FWHM = full width at halve maximum

fq = quality factor

Id = area under the curve of the diamond peak

$\sum_{nd} I_{nd}$ = sum of the area under the curves of the sp^2 phase peaks

3D = three dimensional

AC = alternating current

I_{pa} = peak anodic current

I_{pc} = peak cathodic current

Ag/AgCl = silver chloride electrode

PBS = phosphate buffered saline

μA = microampere

Hz = Hertz

ml = milliliter

mM = millimolar

$K_3Fe(CN)_6$ = potassium ferricyanide

V = Volt

PDMS = polydimethylsiloxane

a.u. = arbitrary units

Preface

The practical work for this research took place in separate institutes and would not have been realized without international cooperation. I like to thank all people involved starting with dr. Frantisek Fendrych and Andrew Taylor who instantly made me feel at home in the Institute of Physics of the Czech Republic. Many hours where spent doing meaningful work and discussing trivial things. When it was time to go home and continue the project at the Institute of Materials Research Lars Grieten took it upon himself to fill that void. For that I thank him as well. Finally I would like show my gratitude to prof. dr. Milos Nesladek who made the experience abroad possible and provided the expertise and guidance to write this document.

Abstract

In the field of biomaterial science many new applications for medicine and biotechnology are achieved through interdisciplinary research. Different materials are used for these purposes. Diamond for instance is known for its superior mechanical and chemical properties but only recently also for its high degree of biocompatibility. Therefore it has become a popular candidate for incorporation in medical devices. This research investigates the applicability of diamond thin film coatings on cardiac stimulation electrodes. To proof this principle wires made of titanium, iridium, platinum/iridium and stainless steel are implemented as these are the materials used for modern day cardiac devices. Growth of nanocrystalline diamond films is accomplished using a. microwave plasma enhanced chemical vapour deposition procedure. Characterization of the thin films is done by Raman spectroscopy while morphology is investigated using scanning electron microscopy. Successfully coated wires of titanium, iridium, platinum/iridium and stainless steel are used to construct electrodes on which electrode functionality analysis performed. A custom built electrochemical cell is used for both electrochemical impedance spectroscopy and cyclic voltammetry to determine changes in electrode behaviour. Results indicate thin films grown on titanium are of superior quality due to strong surface hydrophilicity which fabours seeding while functionality testing of diamond coated electrodes suggests platinum/iridium is the most promising substrate to continue research.

1 Introduction

Biomaterials science is a diverse and interdisciplinary field with an array of applications in medicine and biotechnology while spanning the subject areas of biology, physics, chemistry and materials science. Materials used include metals, ceramics, polymers, glasses, carbons, and composite materials. This work will focus on biomaterials in medicine, more precisely on materials that come into contact with biological systems. For the majority of applications biomaterials are integrated in a device or implant. As these objects can evoke a whole range of negative biological responses from the host, the most important reason for using such materials is to improve biocompatibility.[1] Diamond has emerged as a highly promising new candidate in this regard. Coincidentally heteroepitaxial growth of diamond is also possible on substrates made of metal, making it an interesting coating for bioelectrodes.

1.1 Cardiovascular Medical Devices

From the array of implantable cardiovascular devices this study is limited to pacemakers and Implantable Cardioverter-Defibrillators (ICD), their common factor being electrical stimulation of heart tissue through a bioelectrode. Both are used to treat specific types of cardiac arrhythmias, a set of conditions characterized by abnormal electrical activity in the heart caused by malfunctioning of its intrinsic pacing system. [2] For the device to function effectively the bioelectrode, which is located at the tip of the lead, is passively or actively attached to the cardiac tissue. In case of passive fixation the lead is pushed into contact with the tissue and held in place by tines (Fig.1). Active fixation on the other hand requires tissue penetration by screwing in a retractable metal helix protruding from the lead tip. Though active fixation does induce tissue damage both systems seem to be confronted with similar undesirable effects with regard to biological reactions from the host.[3]

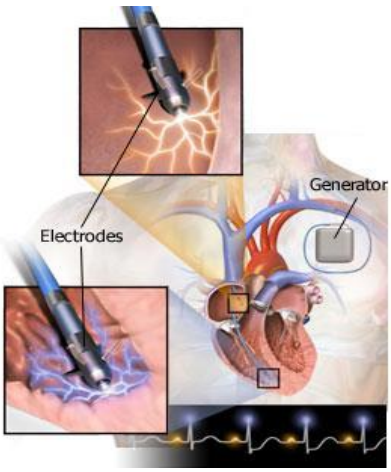

Figure 1: Image of implanted dual chamber pacemaker with passively fixated lead.[4]

1.2 Biological Reactions to a Foreign Body

When the human body is confronted with an implant, a foreign body reaction (FBR) from the invaded tissue is unavoidable.[5,6] Depending on the patients genetic make-up the immunological response can vary between a mild transient infection to an acute graft rejection. The FBR is a special form of non-specific inflammation characterized by a large presence of macrophages which cannot engulf the non-biological material and instead release cytokines that stimulate inflammation and fibrosis. After implantation of the electrode the tissue typically shows an initial acute inflammation which turns chronic. In the subsequent phase of the FBR granuloma tissue arises which will eventually heal through scar-tissue formation leaving a fibrotic cap. When selecting the proper material for a cardiac electrode not only the tissue compatibility but also the haemo- or blood compatibility must be kept in mind. Triggering of the coagulation cascade through adhesion of fibrinogen proteins or activation of platelet cells and the complement system can lead to thrombus formation. The adhesion of fibrinogen proteins can also cause the formation of a biofilm in contact with blood as well as tissue. This layer of microorganisms, mostly bacteria which initially bind to the proteins, proliferates into a slimy conglomeration of cells and extracellular material and causes very persistent infections.

1.3 Biocompatible Materials

Next to sensing, a cardiac electrode also does electric stimulation. Therefore metals with favorable conductive properties are the material of choice. However for implementation in the human body equally important criteria for selection are corrosion resistance and chemical inertness. In case of the former the aqueous and chemically heterogeneous environment of the body could cause fragments of material to crumble off. Contrary to bulk properties smaller fragments can potentially be cytotoxic or evoke an immune response. Chemical inertness on the other hand prevents unwanted and or unfavorable chemical reactions taking place. With these criteria in mind present day manufacturers of cardiac leads have opted for titanium, platinum, iridium or a combination of these as material for electrodes [7]. All have similar merit and the choice depends on which property receives emphasis. Titanium being narrowly superior regarding biocompatibility , platinum regarding resistivity and iridium concerning chemical stability.[8,9]

In recent times however it has come to light that diamond, more precisely diamond in nanocrystalline form, displays even more favorable attributes in terms of biocompatibitilty[10]. In direct comparison to titanium in vitro and in vivo experiments have shown less adhesion of fibrinogen proteins and activation of immune cells[11]. Concerning resistance to bacterial colonization diamond also outperforms titanium

significantly [12]. As for haemocompatibility diamond has shown to have high level resistance to adhesion of platelets and plasma proteins while revealing minimal influence on the coagulation-cascade [13,14]. In addition the intrinsic properties of diamond are ranked highest of all materials for corrosion resistance and chemical inertness.

1.4 Application of Diamond in Medical Devices

The growing number of reported medical applications implementing synthetic diamond is acknowledgment of its unique properties and its potential for improving diagnosis and treatment. The vast array of applications which already exists can be categorized based upon the type of diamond structure or the desired property used. Nanodiamond particles are demonstrated to be useful as drug delivery system but also as a tool for medical imaging. In case of drug delivery the possibility to covalently immobilize drug and targeting biomolecules on the surface of diamond is handily used to treat specific tissue while the fluorescence properties induces by point defects in the diamond crystal are utilized for imaging purposes[15,16]. Diamond in the shape of thin film coatings is also shown to effectively improve existing medical devices through superior mechanical and biological properties. Such is the case for a variety coated joint prostheses and heart valves which report improved functional characteristics[17,18].

For implementation in bioelectrodes the diamond coating must fulfill certain morphological and functional requirements. The former referring to a homogeneous closed film thinner than 100 nm exhibiting reliable adhesion to the cylindrical substrate. To achieve full surface covering the substrate preparation must be optimized.

Adhesion of the film is primarily influenced by the intrinsic properties of the used substrate. In case of metals these properties are the lattice constant, thermal expansion coefficient and degree of carbon uptake at the surface through diffusion. The lattice constant or interatomic distance in the metals crystal roster tends best to be close to that of the diamond crystal. This way interface defects through stacking of atoms or distortions at the phase boundary are kept at a minimum.[19]

Thermal expansion can cause the film to delaminate when cooling down. Carbon uptake by the substrate is unavoidably and will cause an intermediate metal carbide layer to be formed. If this layer is relatively thick and porous, adhesion is compromised as its structural stability is considerably lower than that of pure metal. Both thermal expansion and carbon uptakes is minimized by depositing thin films at relatively low temperatures [20].

As for functionality proper surface morphology ensures biocompatiblity while electric conductivity is regulated through the structural characteristics of the thin films. In undoped diamond films conductivity is possible through 'hopping' which is a tunneling

effect taking place in the sp^2-carbon content. However, signaling of heart tissue by electrical pulses is mediated through changes in electric fields and not by charges crossing the electrode-tissue interface. So to save battery life of a cardiac stimulating device thin film conductivity is not a critical factor. Rather it is preferable to keep film thickness at a minimum as the film will increase the excitation threshold similar to the effect induced by fibrotic encapsulation.[21]

1.5 Research Plan

The ultimate goal of research is to successfully coat a NCD film on cardiac stimulating bioelectrodes for improved biocompatibility. To realize this, optimization of the overall procedure is carried out on relevant substrate materials with cylindrical structure. Namely wires made of titanium, iridium, platinum-iridium alloy and stainless steel.
In the first phase different seeding techniques are compared to obtain the best starting conditions for film growth. Scanning electron microscopy (SEM) is used to assess the nucleation density and spreading homogeneity of seeding. Growth of NCD thin films is done in a custom MWPECVD reactor. Film quality is investigated using raman infrared spectroscopy while for morphology atomic force microscopy (AFM) and SEM is used. If closed thin films of 100 to 200 nm thickness are achieved a second phase of functionality testing is started.
To analyze the electrode characteristics of the NCD coated wires a custom electrochemical cell is built. This setup is then used to perform electrochemical impedance spectroscopy (EIS) and cyclic voltammetry (CV). The former renders information on changes in impedance/resistance at the electrode-electrolyte interface while the latter indicates if redox reactions or charge transfers are taking place.

2 Materials & Methods

Growth of synthetic diamond is possible in a number of ways wherein Microwave Plasma Enhanced Chemical Vapor Deposition (MW PE CVD) is most commonly used. By filling a high vacuum chamber with a controlled gas mixture and inducing a plasma through microwave irradiation chemical deposition of diamond thin films can take place on an array of different substrates. Crucial is the presence of methane and hydrogen gas, the former being a source for carbon and the latter for etching away graphite which is also formed in the process.

2.1 General Principles of Diamond Growth by MW PE CVD

For diamond to grow in a realistic period of time the substrate is first pretreated. This process is called 'seeding' and is marked by the surface being covered with a high density layer of diamond nanoparticles typically smaller than 10 nanometer in diameter. This initial nucleation deletes the disproportionately long time it takes diamond nucleation centers to from spontaneously. Growth on a non-carbon surface can thus start immediately.

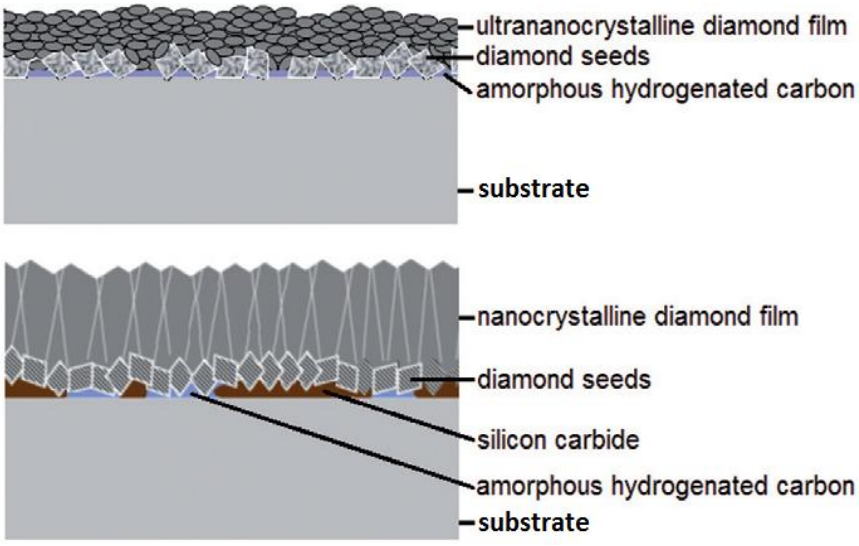

Figure 2: Schematics of growth mechanisms (top) UNCD and (bottom) NCD.[22]

To achieve formation of ultrananocrystalline diamond (UNCD - Fig. 2: top) argon is added to the gas mixture of hydrogen gas and methane. Its presence will prompt the thin film structure to exhibit diamond grains of several nanometers in size held together by an amorphous sp^2-carbon phase through a process called 'renucleation'. Once a carbon layer of diamond, graphite or both is formed argon atoms can efficiently induce the formation of new nucleation centers giving the grown thin film its characteristic UNCD structure.

In the absence of argon the dominant gas is hydrogen and will induce the formation of nanocrystalline diamond (NCD - Fig. 2: bottom). Under these conditions no renucleation takes place and grain size will be proportional to the film thickness due to columnar growth. Formation of sp^3-carbon or diamond continuous on the surface of the seeded particles which grow in size both perpendicular and parallel to the substrate surface. As grains seemingly compete for size the larger ones will eventually cut off their smaller neighbors. This process is called 'van der Drift' growth and as a result the film closes through coalescence while giving it a columnar structure. Increasing film thickness will thus increase grain size eventually reaching a microcrystalline structure.[23]

2.2 Substrate Pretreatment

Deposition experiments are carried out on metal wire substrates of relevant bioelectrode materials which are also compatible with diamond CVD. These are titanium (Ti), iridium (Ir), platinum/iridium (Pl/Ir) and stainless steel (SS).[24-27] Because wires have a similar cylindrical shape compared to electrodes, they are used as a model substrate for proof-of-principle. Specifications and properties are listed in table 1 of the appendix.
As mentioned in paragraph 2.1 pretreatment of the substrate is done through a process called seeding. This introduces the initial nucleation layer on the surface necessary to start growth. The monolayer of diamond nanoparticles defined by its density and spreading. However before actual seeding of nanoparticles (Fig. 3) takes place the surface is first cleaned to remove dust particles. The complete surface can thus undergo seeding which enhanced the potential formation of a closed film. Wire substrates are first rinsed with isopropyl alcohol and wiped down mechanically with optical grade paper and rinsed again. After drying with clean dry air (CDA) ultrasonication for 15 minutes in a bath of isopropyl alcohol follows. Then the substrate is again dried with CDA.

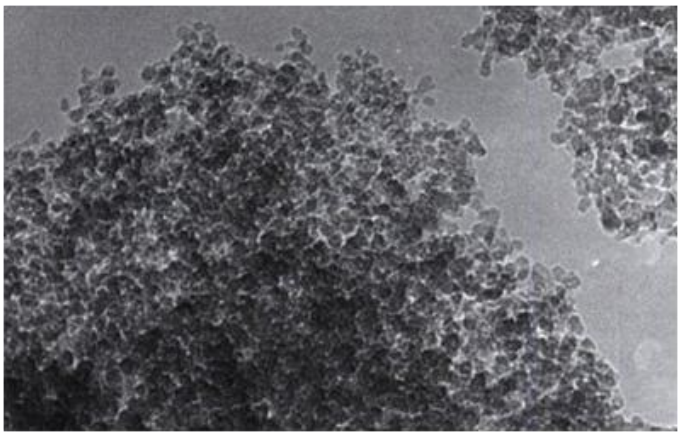

Figure 3: SEM image of clustered diamond nanoparticles.[28]

2.2.1 Preparation of Seeding Solution

The seeding solution or slurry is a suspension of dispersed nanodiamond particles (Fig.X) with an average size of 7 nm and a concentration of 1 mg/l. Osawa detonation diamond is dispersed in deionized water and ultrasonicated for several hours to undo clustering. Subsequently the dispersion is centrifuged to remove larger particles until usable for seeding.

By seeding in solution higher nucleation densities ($>10^{\wedge 11}$ cm^{-2}) are reached compared to mechanical seeding. Apart from being able to seed 3-dimensional structures in solution, no profound damage is done to the surface of the substrate compared to mechanical seeding. This technique namely requires the substrate to be pressed down on a vibrating table while covered with diamond powder.[29]

2.2.2 Seeding Techniques in Solution

The most straightforward way to seed a cleaned substrate is by dip-coating the wire in the seeding slurry. Using tweezers most of the wire is vertically submerged and kept in the slurry for several seconds. The substrate is then pulled upward from the dispersion at a constant speed. A greater speeds results in a thinner covering and vice versa. The seeded substrate is left to dry in ambient air.

A more time consuming method of seeding involves the substrate being submerges in slurry and placed in an ultrasonication bath for a set period of time. Continuing ultrasonic pulses cause the diamond nanoparticles to inflict scratches on the substrate surface which will enhance formation of nucleation centers during initial deposition. Combined with the particles left on the surface after removal from solution a higher nucleation density and homogeneity is achievable. After 15 or 30 minutes of ultrasonication the seeded substrate is also left to dry in ambient air.

As an alternative to the standard methods previously mentioned, seeding of samples is also possible by sweeping a droplet of seeding solution along the surface of the wire. A plastic pipette is squeezed until a stable droplet forms at the tip which is then brought into contact with the wire and moved repeatedly along the surface.

2.3 Microwave Plasma Enhanced Chemical Vapor Deposition

Growth of diamond thin films is realized by using a custom built MWPECVD apparatus (fig.4 left). Compared to standard microwave systems this setup employs high frequency pulses rather than continuous microwave irradiation.[30] The benefit of a high frequency (HF) pulsed system is reduction of input power up to a factor of 50 which directly causes the temperature at which deposition occurs to drop to as low as 450 °C. The underlying mechanism is the non-linear microwave absorption conditions created through HF

pulsing. In strong microwave fields non-linear electron acceleration causes microwave absorption to increase non-linearly with power.[31]

2.3.1 Growth Conditions

As can be seen in the schematic (Fig.4 right) the custom reactor has the same basic design as a standard MWPECVD system excluding the linear antennas for HF pulsing. A ultra high vacuum with active base pressure of 1.001 mBar is maintained through a set of rotary and turbo molecular pumps. A symmetric gas inlet system allows a specific mixture of gas to flow homogeneously through the reactor. For all depositions the gas mixture is comprised of 92% hydrogen (H), 5% methane (CH_4) and 3% carbon dioxide (CO_2). The specific growth conditions at which individual depositions have taken place are listed in table 2 of the appendix.

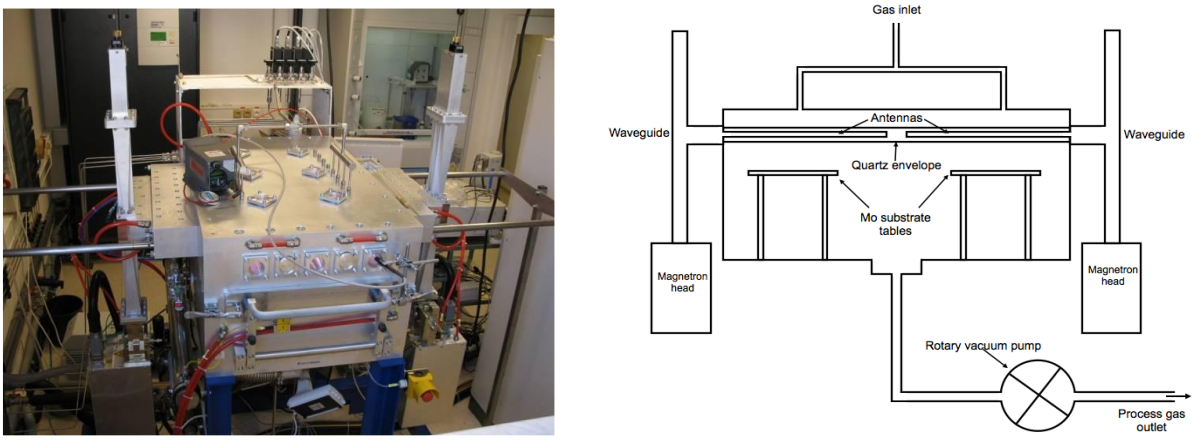

Figure 4: left) Image and right) schematic of custom MWPECVD system

2.3.2 CVD Reaction Process

To induce a local plasma above the substrate table microwaves generated by the magnetron heads are sent by waveguides to the linear antennas which irradiate the gas mixture. The power of the pulses is set to 8 kW at a frequency of 4.54 kHz resulting in an average forward power of 2.45 kW power and an average reflected power of 0.34 kW. The plasma which is comprised of gas molecules, atoms, ions and electrons and is a highly reactive environment necessary to form diamond. Methane gas functions as the main source for carbon radicals. These will form clusters of sp^2- and or sp^3-carbon or in the presence of seeded diamond particle cause immediate growth through stepwise atom addition (Fig.5).

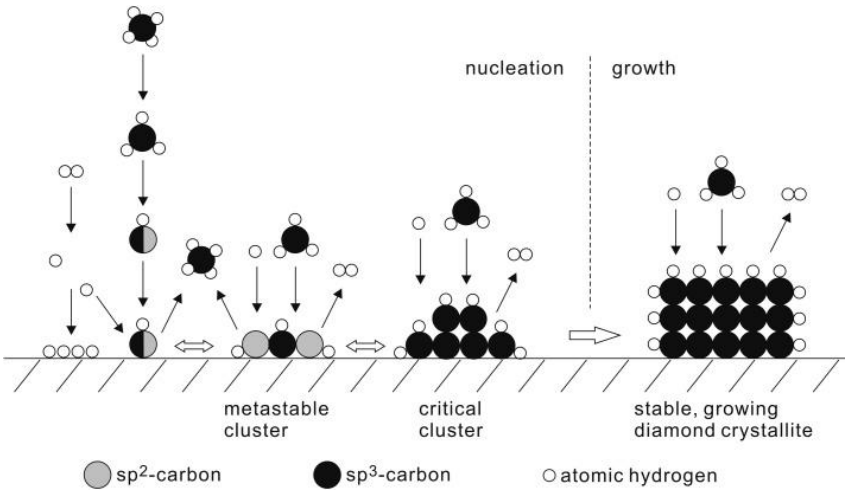

Figure 5: Schematic of reaction mechanism for diamond deposition.[32]

The role of hydrogen gas is the elimination sp^2-carbon through de novo formation of methane. The presence of carbon dioxide stimulates both previously mentioned reactions thus increasing growth rate and phase purity as well as decrease surface roughness [33]. Each deposition runs on average for 6 hours to grow thin films with an estimated thickness of 100-200 nm. The substrates used in every deposition are listed in Table 3 of the Appendix.

2.4 Analysis of NCD Film

After a substrate wire is coated the characteristics of the NCD film are determined. The following techniques are used to investigate chemical composition and surface morphology.

2.4.1 Raman Infrared Spectroscopy

For qualitative chemical characterization spectra rendered by a raman infrared spectrometer are analyzed. The principle of this technique is explained in figure 6. Irradiation of the sample with monochromatic light in the near infrared range induces inelastic scattering through interaction of photons with electrons of bonds and phonons in the thin film. This 'Raman effect' is a Stokes or Anti-Stokes type of scattering depending on a positive or negative energy difference in the bonds or phonons vibrational state after excitation. The resulting changes in intensity for the transmitted light are registered and form the spectrum. Information on both chemical structure and purity of formed carbon compounds are subsequently obtainable through interpretation of intensity, shape and pattern of the spectral peaks. A list of relevant carbon compounds is given in table 1 together with the corresponding wavenumbers or Raman shifts and the range of full width at halve maximum (FWHM) of the peaks.

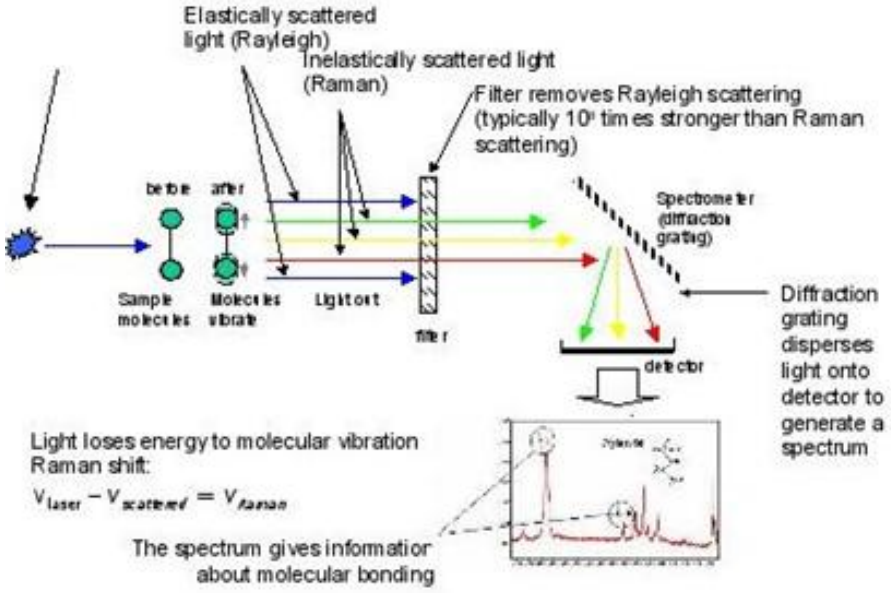

Figure 6: Schematic explaining principles of Raman spectroscopy.[34]

Spectra are acquired with a Renishaw Invia Raman Microscope. The laser with an excitation wavelength of 488 nm is pointed at different positions along the longitudinal axis of the coated wires . Each spectrum is obtained by averaging 20 acquisitions at 10 seconds exposure time.

Table 1: Carbon compounds with corresponding Raman peak characteristics

Carbon type	Wavenumber (cm^{-1})	FWHM (cm^{-1})
Amorphous sp^3-carbon (T-band)	1120-1150	30-100
Hexagonal diamond (Lonsdaleite)	1313-1326	2.8
Diamond	1332.5	1.5-40
Microcrystalline graphite (D-band)	1355	80-400
Amorphous sp^2-carbon (I-band)	1500	350-500
Graphite (G-band)	1520-1610	40-200

Spectral interpretation starts by assigning proper labels to each peak so as to specify what type of carbon compounds have formed during deposition. For a more detailed characterization the phase purity and crystalline quality of the thin films are determined as well through peak fitting Gaussian functions in the spectra using Originlab software. This enables the area under the curve and FWHM of peaks to be quantified.

The phase purity which is defined as the diamond/graphite ratio can be calculated by applying the following formula wherein *fq* is confusingly named the quality factor (eq.1) [35 Fortunato].

$$fq = \frac{75 \times I_d}{75 \times I_d + \sum_{nd} I_{nd}} \times 100$$

(equation.1)

In the equation I_d refers to the area under the curve of the diamond peak and $\sum_{nd} I_{nd}$ to the sum of the area under the curves of the sp^2 phase peaks. The factor 75 corrects for the more effective Raman scattering of sp^2 structures [36]

The crystalline quality, not to be confused with *fq*, is an indicator of the quality specific of the diamond content. It is determined more straightforward by measuring the FWHM of the diamond peak normally centered at 1332.5 cm^{-1}. Due to temperature and lattice strain effect it is possible for the diamond peak to be shifted [37].

2.4.2 Atomic Force Microscopy

To analyze the surface morphology of samples AFM is used. This technique is able to render 3-dimentianal digital profile of the surface's roughness with nanometer resolution. The principle of this technique is explained in figure 6.

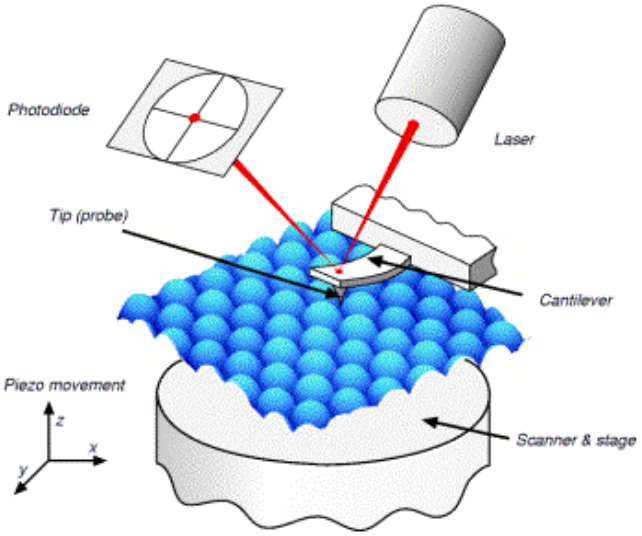

Figure 6: Schematic explaining principles of AFM.[38]

A sharp tip only several atoms thin and protruding from a cantilever scans the surface in serial sequence. A laser is aimed at the top surface of the cantilever and continuously deflects its light into a patch of photodiode sensors. With varying heights of the surface structure the cantilever deviates changing the angle of laser light deflection which is subsequently registered by different photodiodes. The resulting 3D digital profile is a height distribution of the sample's surface and can give information on homogeneous film covering and film thickness. It's also possible to measure distances across the surface in the nanometer range. A NTEGRA Prima NT MDT system is used in non contact mode to investigate surface roughness of clean uncoated substrate wires.

2.4.3 Scanning Electron Microscopy

An alternative tool to investigate surface morphology of samples is the scanning electron microscopy. Grayscale visual images of the sample surface are produced at nanometer resolution. by scanning the sample surface with a high energy electron beam in a raster-like pattern. The principle of this technique is visualized in figure 7. As the electrons from the beam interact with the atoms in the surface, signals are produced by scattered electrons and electromagnetic waves. Through detection of these signals information on surface topography is obtained and a digital image with a high depth of field can be reconstructed. The NCD coated wires are fixed to the substrate table inside a vacuum chamber during analysis. Images with a magnification factor ranging from 800 to 20000 are made from positions along the shaft and the tip of the coated wire.

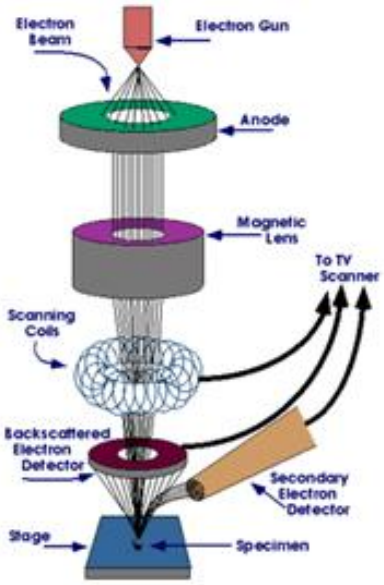

Figure 7: Schematic explaining principles of SEM.[39]

2.5 Functional Analysis of NCD Coated Electrodes

By modifying the surface of an electrode through NCD coating its functional properties are influenced. To investigate the induced changes electrochemical impedance spectroscopy and cyclic voltammetry are implemented.

2.5.1 Electrochemical Impedance Spectroscopy

Impedance is roughly described as the resistance of a system towards an applied alternating current (AC). To determine the impedance at the electrode-electrolyte interface EIS is the technique most commonly used. In figure 7 the general equivalent circuit for this type of system is shown with its components, namely the ohmic resistance of the electrolyte solution (R_s), the Warburg impedance resulting from the diffusion of

ions from the bulk electrolyte to the electrode interface (Z_W), the double layer capacitance (C_{dl}) and the electron transfer resistance (R_{et}) if a redox couple is present in the electrolyte solution.

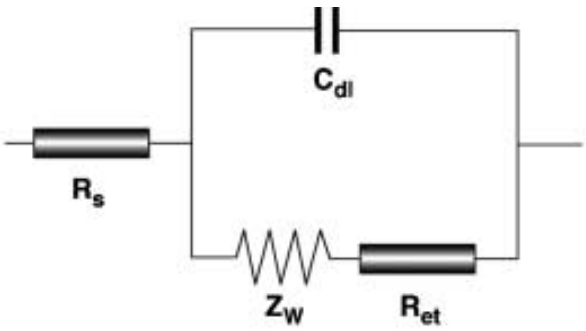

Figure 8: General equivalent circuit for electrode-electrolyte interface in EIS.[40]

A small amplitude sinusoidal voltage signal is applied to the submerged electrode while the frequency is varied according to a set interval of values. The resulting current response is measured from which the impedance is calculated as the ratio between the voltage phasor [$U(j\omega)$] and the current phasor [$I(j\omega)$] of the system (Eq.2).[41] The complex impedance can also be presented as the sum of its the real [$Z_{re}(\omega)$] and imaginary [$Z_{im}(\omega)$] components, mainly originating from the resistance and capacitance of the system.

$$Z(j\omega) = \frac{U(j\omega)}{I(j\omega)} = Z_{re}(\omega) + jZ_{im}(\omega); \quad \text{where } \omega = 2\pi f$$

(Equation 2)

The generated data is graphically presented in Bode plots of modulus and phase. The former plots the absolute value impedance in function the frequency while the later plots the negative phase of the impedance in function of the frequency.

2.5.2 Cyclic Voltrammetry

To detect redox reactions and charge transfers at the interface of an electrode and electrolyte CV is employed. Cyclic voltammetry differs from linear voltammetry as the applied potential is sweeped back and forth between two set values while current is being measured. Usually the potential is scanned back and forth between a positive and negative value at a set constant speed. When the original starting value is reached again one cycle is complete. Measured data is plotted in a voltammogram which has a characteristic 'duck'-like shape (Fig.9) if a redox couple is present.

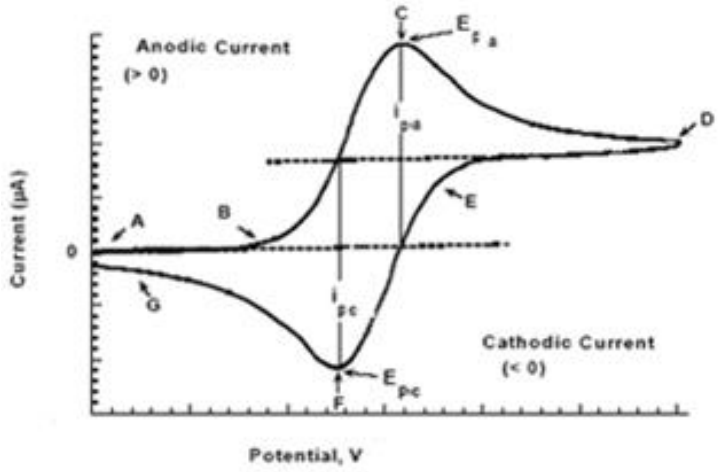

Figure 9: Theoretic example of a cyclic voltammogram[42]

As the applied potential increases the current does as well until the peak anodic current I_{pa} is reached and the electrolyte undergoes reduction. The current eventually steadies as all ions at the interface are depleted and the process now is diffusion limited. Subsequently when the potential decreases and reaches the peak cathodic current I_{pc} the process is reversed and the electrolyte undergoes oxidation. The current again steadies creating two similarly shaped peaks typical of a reversible redox reaction.

2.5.3 Measurements in Electrochemical Cell

To perform EIS and CV a custom electrochemical cell (Fig. 10) is used which has a three electrode setup. The cell is constructed using a commercially available glass jar and a custom made Teflon scaffolding plug. The plug contains two aligned sets of three holes which allow for three electrodes to be fixed in a stable and reproducible position within the setup. The different types of electrodes used are a silver chloride (Ag/AgCl) reference electrode, a platinum counter electrode and a working electrode made from a NCD coated wire.

The working electrodes are constructed by fixating the NCD coated wires partially into teflon tubes of 1mm diameter using polydimethylsiloxane (PDMS) at the edge of the tube. On the other side of the tube electrical copper wire is inserted until connected with the uncoated side of the substrate wire. The rest of the tube is then filled with silver based conductor paste to insure a proper electrical connection.

All electrodes are individually connected to a potentiostat device (Iviumstat Electrochemical Interface, Ivium Technologies) for data collection. This device is operated with Iviumsoft software run by a laptop computer. The data is subsequently processed with Excel and Originlab software.

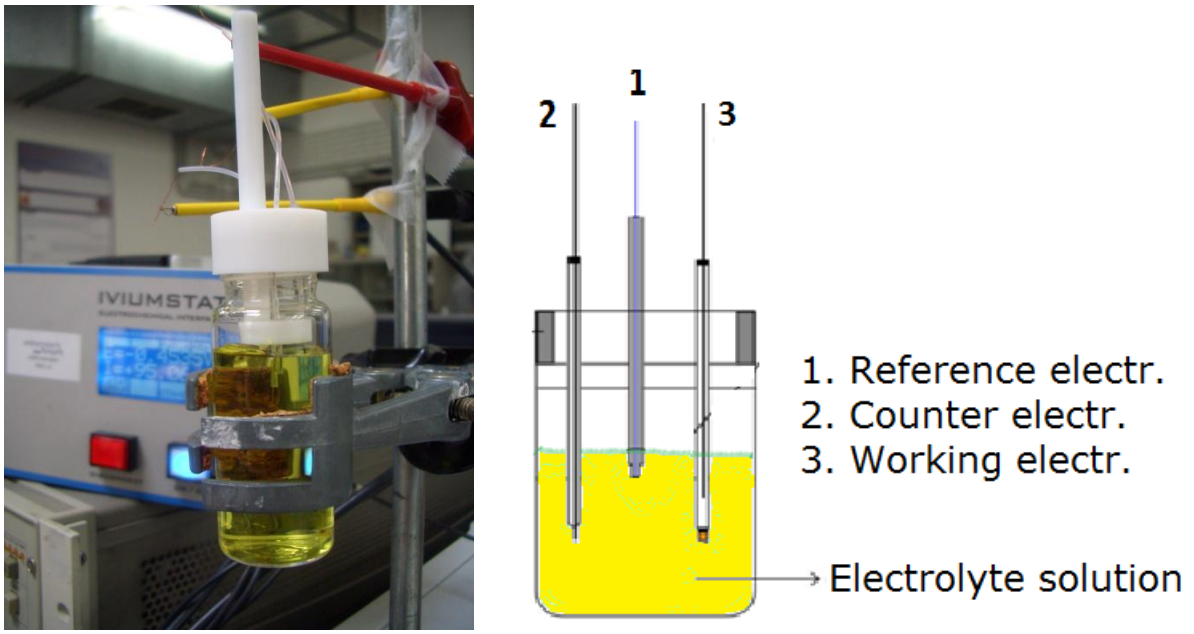

Figure 10: Left) image and right) schematic of three electrode setup in $K_3Fe(CN)_6$ solution

During EIS the Ag/AgCl reference electrode is disconnected and the current to calculate the impedance is measured between the working and counter electrode. The electrolyte solution is 16ml phosphate buffered saline (PBS) which has an osmolarity and ion concentrations that closely match that of the human body. The frequency range is set to sweep from 100kHz to 0,1Hz.

During CV all working electrode samples are measured in an electrolyte solution of 16ml PBS and subsequently in 16ml of 10 mM potassium ferricyanide $K_3Fe(CN)_6$ solution. Potassium ferricyanide is used to increases the redox potential of the solution and acts as an electron transfer agent. The potential range is set to sweep from -1V to 1V at a speed of 0,1V/s. The potential which is applied at the working electrode is a relative value which is compared to the reference electrode. The resulting current flowing through the counter electrode is the one measured. Each working electrode sample undergoes a second series of CV analysis in both electrolyte solutions after the tip of the NCD wire electrode is dipped in polydimethylsiloxane (PDMS). This waterproof silicone is used to cover up the surface area at the tip of the substrate if it is insufficiently coated with NCD.

3 Results & Discussion

During the initial stage of research when fine tuning of the seeding process had taken place SEM was not available to see if a monolayer of diamond nanoparticles was formed at the substrate surface. For that reason raman infrared spectroscopy is used as an alternative technique.

3.1 Substrate Pretreatment

Pretreatment of the substrate is realized by cleaning the surface with isopropyl alcohol and subsequently seeding it in solution by one of three techniques. These are dipping the wire in seeding solution, seeding in an ultrasonicated bath of seeding solution for 10 minutes and sweeping a droplet of seeding solution with a pipette along the wire. As CVD deposition time is only 6 hours no diamond will form unless seeded nucleation centers are already present through seeding. So by checking the raman spectra for a diamond peak at 1332,45 cm^{-1} the applicability of the different methods of seeding can be verified.

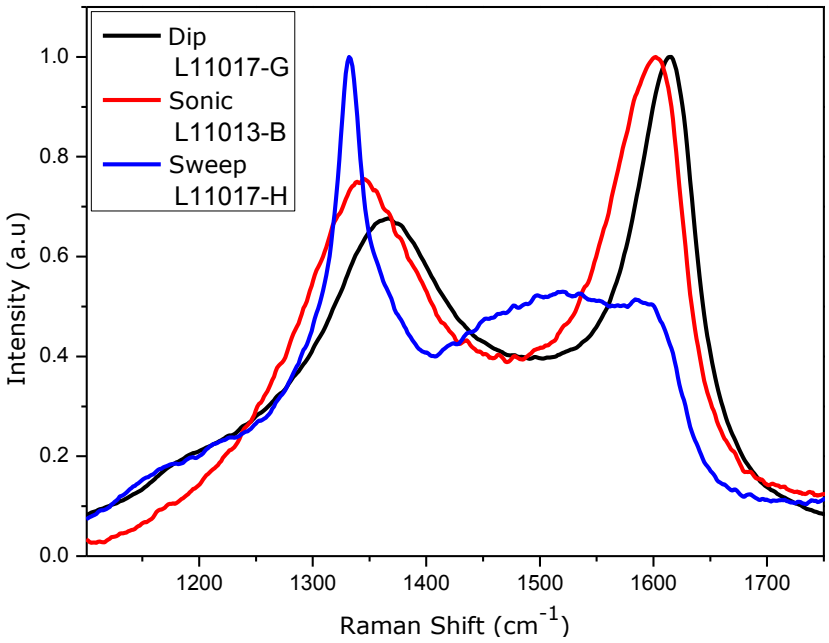

Figure 10: Raman spectra of three different methods of seeding

The three raman spectra seen in figure 10 each represent a different type of seeding method used. Of those only sweeping the substrate wire with a drop of seeding solution on the tip of a pipette renders the desirable outcome as this is proven through the presence of a diamond peak at wavenumber 1332,45. For the methods of dip coating and sonic seeding similar negative results are observed. In both cases only sp^2-carbon is formed during CVD deposition as peaks located around 1350 cm^{-1} 1600^{-1} at are both assignable to different forms of graphite. In theory all methods of seeding described here

should be effective as the metals used as substrate are all hydrophilic. However the water based seeding solution only wetted the substrate wires after intense sweeping with a droplet which could mean that unwanted microfluidic effects come into play as the wire diameters are in the sub-millimeter range.

3.2 Optical Characterization by Raman Spectroscopy

When a substrate is exposed to a microwave induced plasma of hydrogen, carbon dioxide and methane, different forms of carbon are able to deposit. To characterize which types of carbon are present and to estimate their relative content raman infrared spectroscopy is implemented. Each metal used as substrate is discussed separately by examining four raman spectra obtained from four different positions along the length of the shaft of the metal wire. Peak fitting is attempted on all spectra but only successful on two spectra per metal due to software limitations.

3.2.1 Raman Spectroscopy NCD Coated Stainless Steel

The four raman spectra shown on figure 11 all have an almost identical pattern which makes it able to discuss them as one. The most pronounced peak is visible around 1332,45 cm^{-1} indicating that diamond is strongly represented in the deposited thin film. The small shoulder named the D-band, on the right-hand side of the diamond peak at around 1350 cm^{-1}, is due to a small amount of microcrystalline graphite being present. The peaks centered at 1500 cm^{-1} and 1600 cm^{-1} signal the presence of more sp^2-carbon. The former is labeled as the I-band while the latter is the G-Band. They represent the amorphous sp^2-carbon and standard graphite respectively.

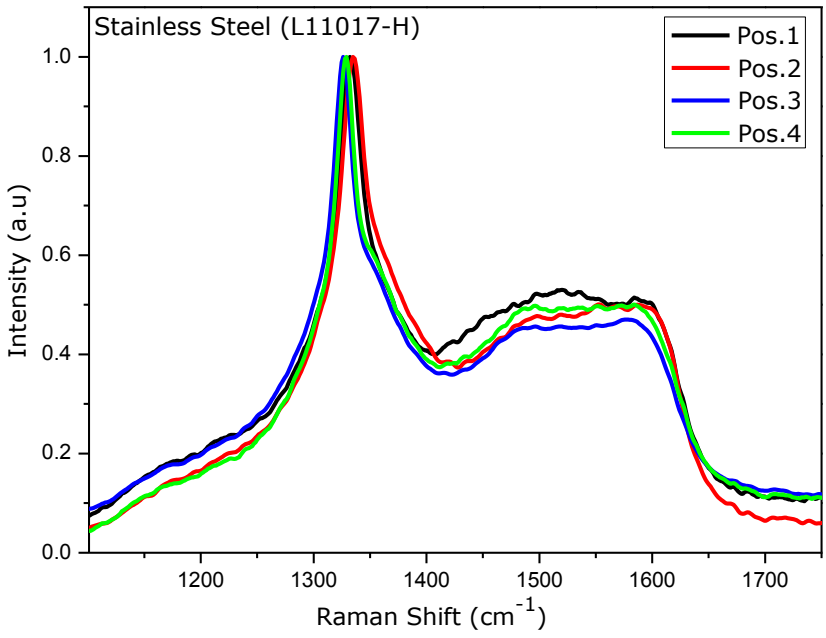

Figure 11: Raman spectra of NCD coated stainless steel

The diamond peaks originating from four different positions on the coated stainless steel wire do not overlap precisely at wavenumber 1332,45 which is the listed value for pure single crystal diamond. Small shifts of several wavernumbers are caused by stresses in the thin film as the SS substrate has different lattice constants due to the different metals incorporated in this alloy. That the spectra taken at four different positions on the substrate have an almost identical pattern suggest that the film is homogenous along the wire regarding composition.

The peak fitting procedure (Appendix fig.5,6) performed on spectra of position 1 and 2 estimates the sp^3/sp^2 or diamond-to-graphite ratio to be 81,45% and 79,99% respectively, while the FWHM of the diamond peaks is estimated to be 35,50 cm^{-1} and 38,65 cm^{-1}. These FWHM values fall within the arbitrary range but deviate quit strongly from the more ideal value of 2. This would indicate that the film is of lesser quality due to possible incorporation of impurities. More likely however, it is because of the nanocrystalline nature of the film which tends to be less pure then single crystal diamond due to the sp^2-carbon content.

3.2.2 Raman Spectroscopy NCD Coated Titanium

The four spectra shown in figure 12 show a roughly similar overall pattern with some minor peak intensity variations. The diamond peak is the most dominant peak in all spectra while position 4 has a more pronounced microcrystalline graphite shoulder. The I-band at around 1500 cm^{-1} registers a higher intensity compared to the D-band at around 1600 cm^{-1} for position 2 and 3 while for position 1 and 4 peak intensity is roughly the same. The amorphous sp^2-carbon to graphite ratio is thus higher in positions 2 and 3.

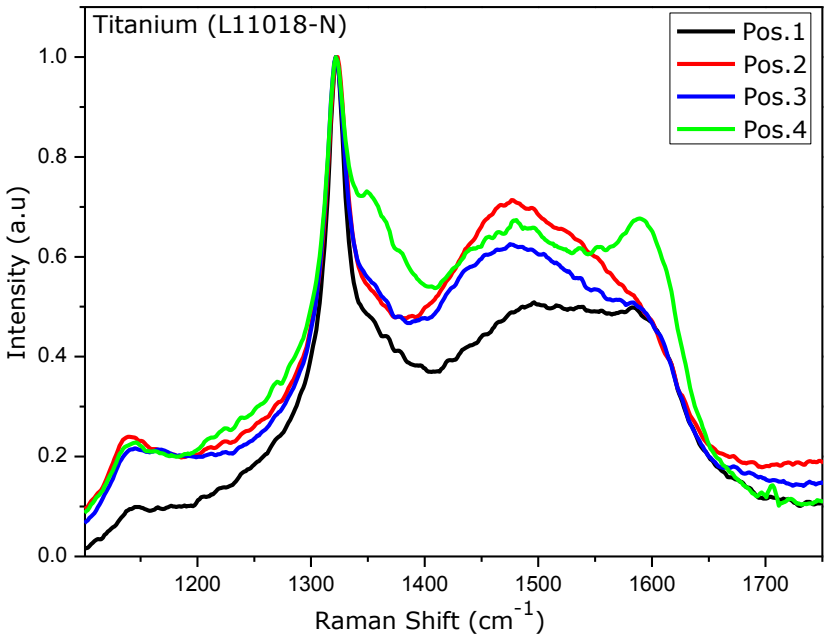

Figure 12: Raman spectra of NCD coated titanium

Each spectrum also contains a small peak named the T-band at about 1140 cm^{-1} which means amorphous sp^3-carbon is formed during deposition as well. Also all sp^2 related peaks for position 1, namely the D-,I- and G-band, register lower intensities as compared to the more similar other three spectra.

The diamond peaks of all four spectra have a high degree of overlap which would indicate that the level of stress is similar throughout the film. The varying overall pattern of the four spectra means that the composition of the film varies slightly as well depending the position. Peak fitting (Appendix fig.7,8) done on the spectrum of position 4 rendered an estimate diamond-to-graphite ratio of 74,38% which is considerably less compared to an estimate ratio of 82,73% for position 2. However position 4 is located at the tip of the wire which could mean the lower sp^3/sp^2 ratio is coupled to a seeding problem (see SEM results) which could explain the shift in composition. The estimated FWHM for the diamond peaks of position 2 and 4 are 37,06 cm^{-1} and 30,95 cm^{-1} which are acceptable according to literature.

3.2.3 Raman Spectroscopy NCD Coated Iridium

The four spectra shown in figure 13 roughly exhibit a similar pattern with some deviations in the spectra of position 3 and 4. The diamond peak is omnipresent and also the most dominant in all spectra. A stronger intensity is regarded for the D-band compared to the I-band for all spectra except position 3.

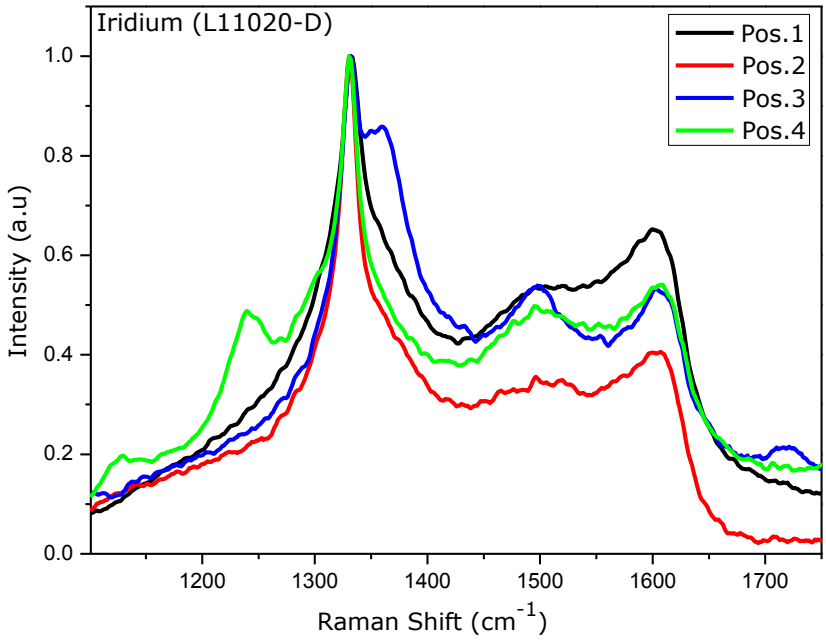

Figure 13: Raman spectra of NCD coated iridium

For position 3 the D-band is also an exception as it is a peak with strong expression while in the other spectra there is only a hint of a shoulder visible. The spectrum of position 4 also registers peaks at around 1140 cm^{-1} and 1250 cm^{-1}.

The diamond peaks of all four spectra overlap to a high degree suggesting the level of stress in the film is homogeneously distributed. As the overall pattern of the spectra are similar, the composition of the film is homogeneously distributed as well. Peak fitting (Appendix fig.9,10) for spectra of position 1 and 2 estimates the diamond-to-graphite ratio to be 77,06% and 82,42% respectively which would support this observation. The estimated FWHM values for the diamond peaks of position 1 and 2 are 36,61 cm^{-1} and 32,88 cm^{-1} which are acceptable according to literature.

3.2.4 Raman Spectroscopy NCD Coated Platinum/Iridium

The four spectra shown in figure 14 have similar overall patterns which overlap roughly with the exception of position 4. The diamond peaks are present for all four positions and register the highest intensity. A minor D-band shoulder is visible while the I- and D-band have relatively low levels of expression compared to the diamond peak with the exception of position 4.

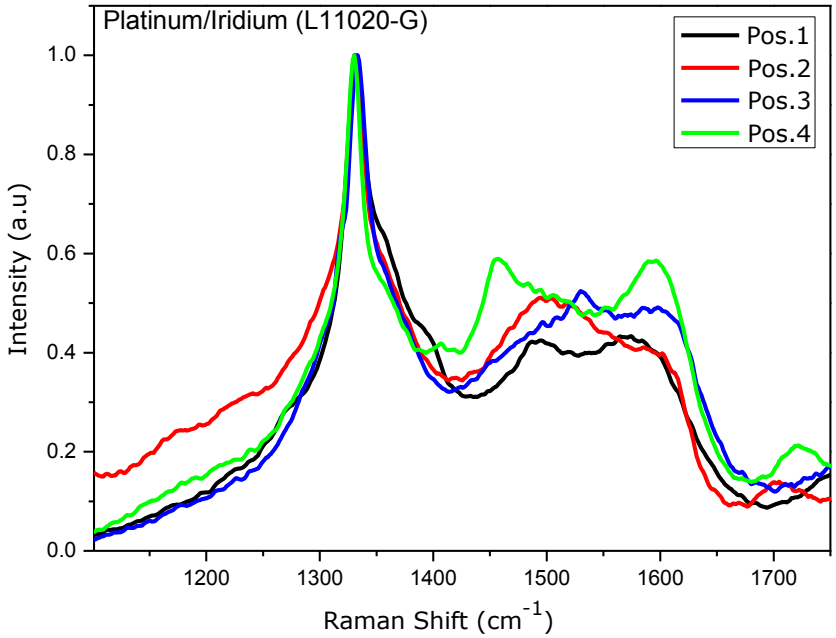

Figure 14: Raman spectra of NCD coated platinum/iridium

The diamond peaks of all four positions overlap roughly indicating minor differences in the level of stress throughout the film. The overall pattern of the spectra roughly overlap as well which points at a homogenous composition throughout the film. The partial exception is the spectrum of position 4 which registers a higher relative sp^2-carbon content. Unfortunately peak fitting (Appendix fig.11,12) was only successful on spectra of

position 1 and 2 which estimate the diamond-to-graphite ratio to be 77,66% and 78,89% while the values for the FWHM of the diamond peaks are estimated to be 28,93 cm^{-1} and 30,25 cm^{-1}.

Raman spectroscopy revealed growth of NCD is possible on cylindrical metal substrates of stainless steel, titanium, iridium and platinum/iridium. Films on all four substrates show homogenous distributions regarding composition. Minor stress level differences are seen in films grown on stainless steel substrate probably due to the varying lattice constants of the different metals which make up this alloy. Peak fitting estimated the diamond-to-graphite ratio of the films on all substrates to lie between 74,38% and 82,72% which is consistent with the fact that all films are grown under the same CVD conditions. The same can be said about the FWHM values for the diamond peaks which lie between 38,65 cm^{-1} and 30,95 cm^{-1}. The peak fitting procedure is however sensitive to errors so all calculated values should be seen as rough estimates.

3.3 NCD Film Morphology

To investigate the topography and structural integrity of the deposited thin films only SEM is used. For this particular research AFM is not applicable as the figures 1-4 in the Appendix indicate. Spots of 5x5 µm on clean uncoated substrates are analyzed with AFM and show the surface of the metal wires to be relatively rough. Stainless steel (Appendix fig.1) has a 102,9 nm difference in height between registered minimum and maximum with an average height difference of 46,1 nm measured. Titanium (Appendix fig.2) has a difference of 820,3 nm between minimum and maximum with an average height difference of 373,9 nm. The difference between minimum and maximum for iridium is 156,8 nm while average height difference measured is 78,8 nm. For platinum/iridium the difference between minimum and maximum is 86,5 nm and the average height difference is 49,9 nm. The NCD thin films which are grown have an estimated thickness of 100-200 nm with a rough (nanocrystalline) surface of their own. Under these circumstances AFM rendered information on coated wires is inconclusive.

3.3.1 SEM NCD Coated Stainless Steel

The images seen in figure 15 both reveal a thin film is deposited on the SS wire. At a magnification of 20000x the diamond nanocrystal pattern on the surface can be slightly distinguished on both the left and right image. However without raman analysis it is inconclusive. On the left image of figure 15 the rough underlying topography of the SS wire is still visible. The surface defects as well as the smoother surface areas are coated with a continues film. On the right image of figure 15 which is taken at another position on the wire the film is of an overall lesser quality compared to the image on the left. The

surface defects of the SS surface are mirrored by defects in the overlying coating while the smoother areas of the wire are not coated with an equally smooth film. There are also profound cracks along the surface of the film visible which are caused when the film can no longer cope with internal stresses.

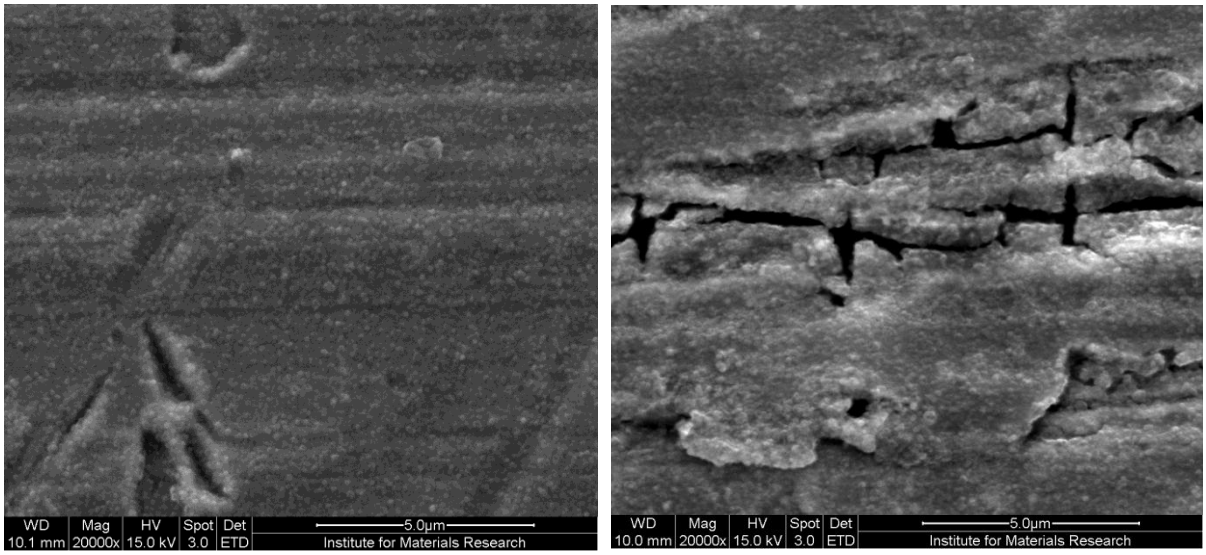

Figure 15: SEM images of NCD coated stainless steel wire (LL11017H): left) and right) spot on shaft at 20000x magnification.

The tip of the SS wire is seen in the SEM image of figure 16. At a magnification of 800x the nanocrystalline structure of the film's surface is not visible. It does however reveal that the surface is not coated with a continuous film at this part of the wire. Some larger patches of continuous film are visible at the bottom and some small irregular spots at the top. This is a result of insufficient seeding which is problematic at the tip of the wire due to microfluidic effects.

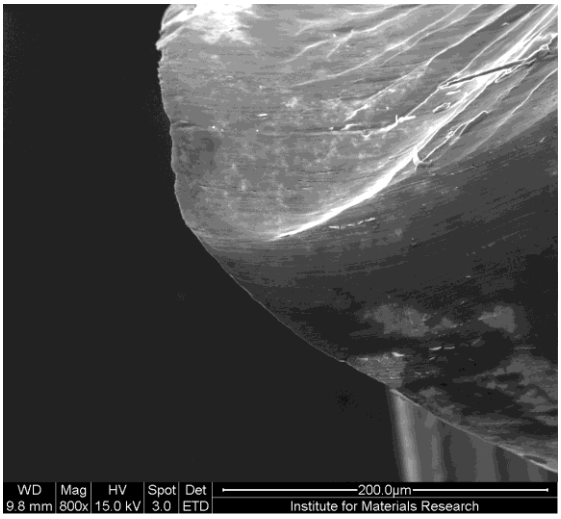

Figure 16: SEM image of tip NCD coated SS wire (L11017H)

3.3.2 SEM NCD Coated Titanium

On both SEM images of figure 17 it is shown that a thin film is deposited on a titanium wire substrate. The surface seems to have a diamond nanocrystal structure on both images but due to substrate roughness SEM results alone are not definite. The left image of figure 17 is taken at magnification 5000x and shows a high degree of film continuity even though titanium has the roughest topography all metal substrates used. Defects such as pits, hills and sharp edges are all able to be coated. This is confirmed by the right image of figure 17 which is taken at a magnification of 20000x. The presumed nanocrystals seen at the surface of the film are sharper defined and packed more densely together compared to coated SS. It could indicate that seeding reaches a higher nucleation density on titanium as substrate, which is plausible giving the strongly hydrophilic surface of this material.

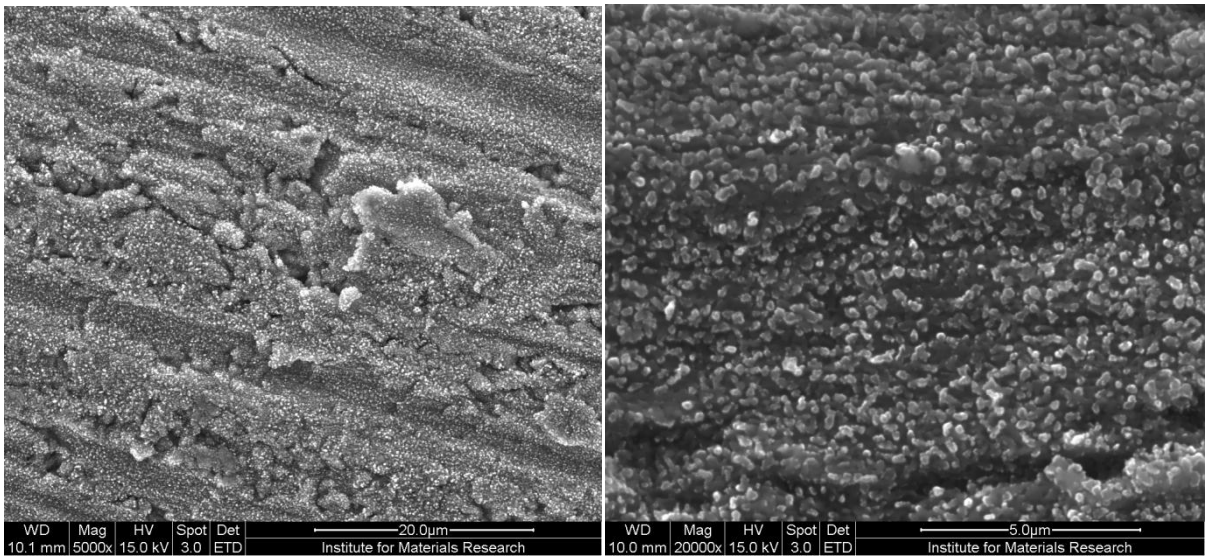

Figure 18: SEM images of NCD coated titanium wire (L11018O): left) and right) spot on shaft at 5000x and 20000x magnification resp.

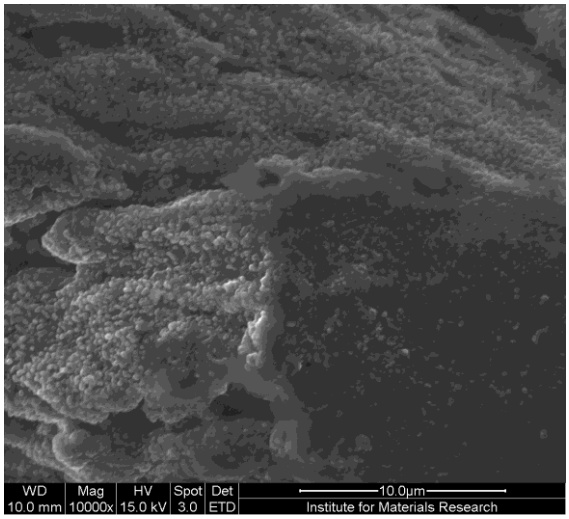

Figure 18: SEM image of tip NCD coated Ti wire (L11018O)

The image seen in figure 18 is taken at magnification 10000x and shows the tip of the wire. The film has a similar surface morphology and continuity compared to images taken along the shaft. Favorable seeding conditions created by strong hydrophilic nature of the surface thus facilitates deposition of a thin film at the tip resulting in less uncovered areas.

3.3.3 SEM NCD Coated Iridium

The SEM images shown in figure 19 both confirm thin film deposition on iridium as substrate. The nanocrystal structure of the surface is difficult to distinguish with certainty at magnification 20000x. The seize and distribution of the deposited material is highly irregular with cauliflower-like clusters protruding from the surface. These clusters take that particular shape when the sp^2 content is heightened as this is the material that makes up the encapsulating grain boundaries. The irregular cluster density distribution and the absence of a continuous film in the defects of the substrate surface indicate homogeneous seeding is less straightforward. This is confirmed by the image on the left in figure 19 which is taken at magnification 5000X. The areas on the surface containing the more profound defects do not coat with a continuous NCD film resulting in a relatively large density of pinholes.

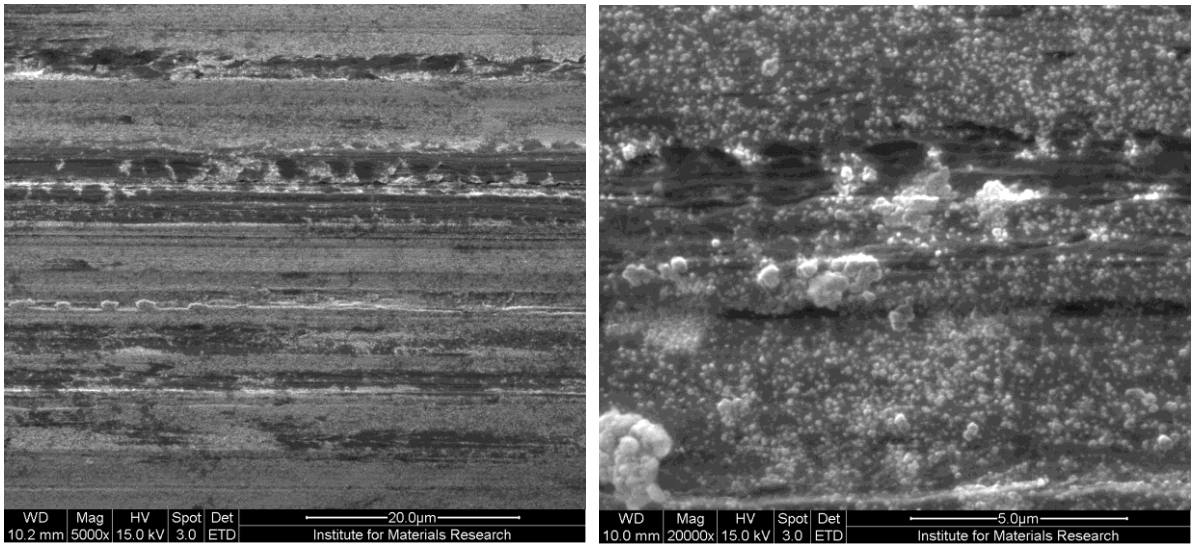

Figure 19: SEM images of NCD coated iridium wire (L11020D): left) and right) spot on shaft at5000x and 20000x magnification resp.

The tip of the Ir wire is seen in figure 20 at magnification 3000x. The topography of the substrate surface is irregular and strongly deformed when the substrate wire was cut with pliers. Small isolated areas of the surface seen in the centre and the bottom of the image are coated with thin film. The surface is clearly not continuously coated while the deformed structure of the substrate combined with the darker patches visible suggests parts of the film are delaminated.

Figure 20: SEM image of tip NCD coated Ir wire (L11020D)

3.3.4 SEM NCD Coated Platinum/Iridium

The SEM images seen in figure 21 confirm the deposition of a thin film on Pl/Ir substrate. The presumed nanocrystal structure at the surface of the film is barely distinguishable on both images. At magnification 20000x it is unclear if the surface defects of the substrate are coated with a continuous film. Smoother areas of the substrate surface also exhibit uncoated patches which suggest that the outcome of seeding on this type of metal is mediocre. The left image of figure 21 corroborates this assessment as smooth areas show partial coating with NCD. The overall smoothness of the metal substrate is however reflected in the surface of the film.

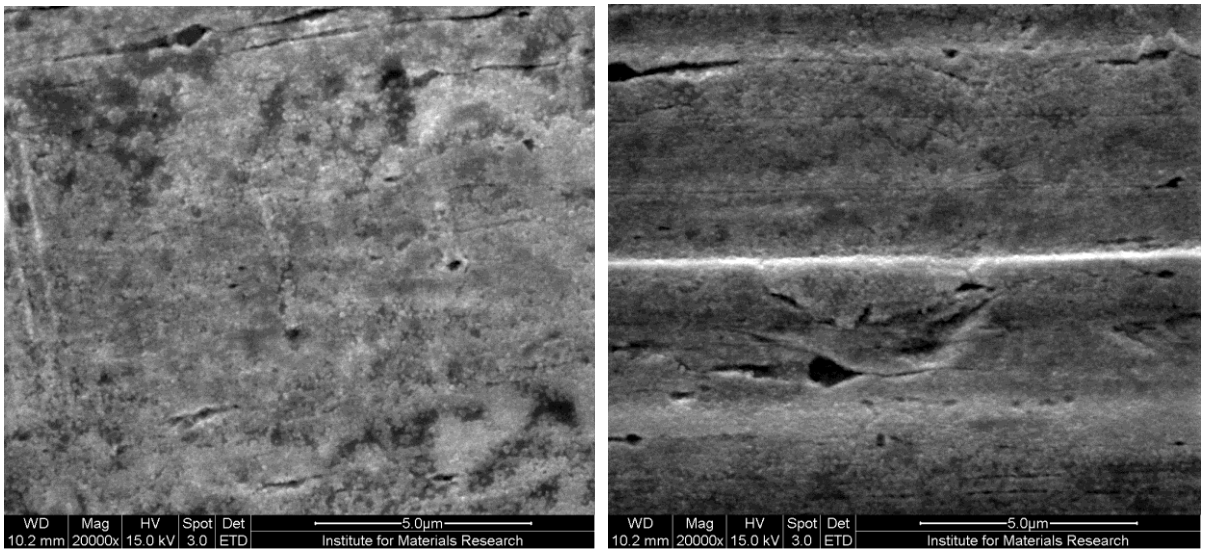

Figure 21: SEM images of NCD coated platinum/iridium wire (L11020G): left) and right) spots on shaft at 20000x magnification.

The tip of the pl/Ir wire seen in figure 22 shows to be partially coated with a thin film. At magnification 10000x no nanocrystal surface pattern can be distinguished in the coated areas. Pinholes are randomly distributed throughout the coated areas while signs of delamination are visible in the bottom of the image where the substrate surface is strongly deformed due to the cutting of the wire with pliers.

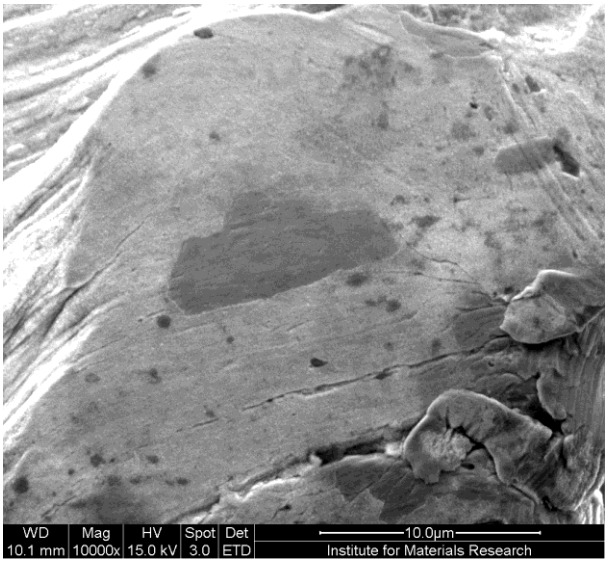

Figure 22: SEM image of tip NCD coated Pl/Ir wire (L11020G)

The collective results of SEM analysis show all metal substrates to be coated with a thin film. The typical surface pattern of NCD is vaguely recognizable but without raman spectroscopic analysis classification of the thin film as NCD would be inconclusive. In all cases the shaft of the wire renders the highest probability of forming a continuous thin film when compared to the tip of the wire. Titanium is the exception as a homogeneous film can form on any area of the wire. A major contributing factor for this is the pronounced hydrophilic character of its surface which provides favorable conditions for seeding. It is also the reason why the coating on titanium has the most pronounced surface pattern that hints at NCD. On titanium the film also continuously covers surface defects and has a homogeneously distributed surface roughness. On iridium, platinum/iridium and stainless steel it is also possible to achieve continuous coatings along the shaft. There are however cracks visible on along the surface of coated SS due to excessive internal stresses which are also confirmed by raman analysis (fig.11). These stresses are generated by the different lattice constants of the different metals which make up the alloy. Coating of the tip is problematic for SS, Ir and to a lesser extent for Pl/Ir substrate due to less favorable seeding conditions caused by mediocre surface hydrofilicity and unfavorable microfluidic effects due to the wire diameter lying in the sub-millimeter range. As a result, surface area coverage at the tip of the wire is low and

may have to be resolved in an alternative manner when analyzing functionality as an electrode.

3.4 Functional Analysis of NCD Coated Electrodes by Electrochemistry

In order to investigate the functionality of NCD coated electrodes electrochemical impedance spectroscopy and cyclic voltammetry are applied through use of a custom built electrochemical cell. The coated electrodes are made by from coated substrate wires which are fixated in Teflon tubing and electrically connected to copper wire by silver based conduction paste in the tube.

3.4.1 Electrochemical Impedance Spectroscopy of NCD Coated Electrodes

In figure 23 all four substrate types (Ti, Pl/Ir, Ir and SS) are represented by their respective Bode plots which show the modulus of the impedance in function of frequency. Both axis are in logarithmic scale. A complete frequency sweep contains 6 decades (0.1 Hz to 100 kHz). In all the cases black represents the uncoated and blue the diamond coated samples. There is a good agreement between the modulus plots (Figure 23 b and c) for the Ir and Pt/Ir.

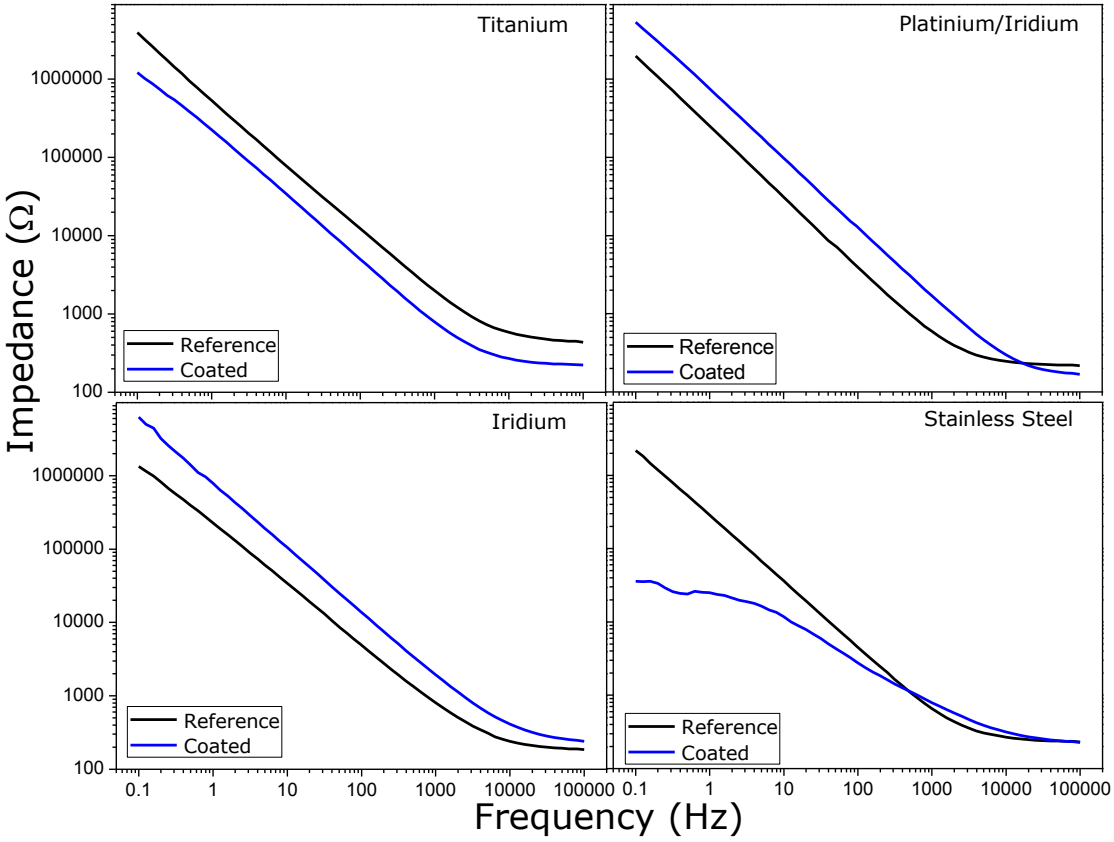

Figure 23: EIS Bode plots of the modulus of uncoated reference and coated electrodes in PBS electrolyte solution; Ti (L11018O), Ir (L11020D), Pl/Ir(L11020G), SS(L11018M)

In both cases coating of the electrode with NCD induces an upward shift of the graph which exhibits the same slope. The phase plots in Figure 24 show that the phase is shifting towards higher frequencies, indicating a decrease of the electrolyte-electrode interface (due to coating of the metal electrode). The NCD coating is not boron doped, and will therefore have a very high resistivity and will not contribute to the electrochemical behavior of the electrode. Also, the coating with NCD on the metal causes the effective surface area in contact with the metal-electrolyte to decrease, and therefore shift the phase back to higher frequencies.

In case of titanium a better coating is obtained and a similar result would be expected due to similarities between metal properties (Appendix table 1). From the modulus no obvious differences are seen, but the phase shows in the low frequency a clear difference between the reference and coated sample. The phase behavior is different before and after coating, and this could indicate that possible oxidation of the titanium is happening during the impedance measurement. This effect completely disappears when the electrode is coated. It raises the suspicion that impedance decreased instead of increased because the coated electrode was possible deeper submerged in solution compared to the uncoated reference electrode. This would namely cause the contact area at the electrode-electrolyte interface to increase. The decrease in contact area through partial thin film coating would in this case be outweighed

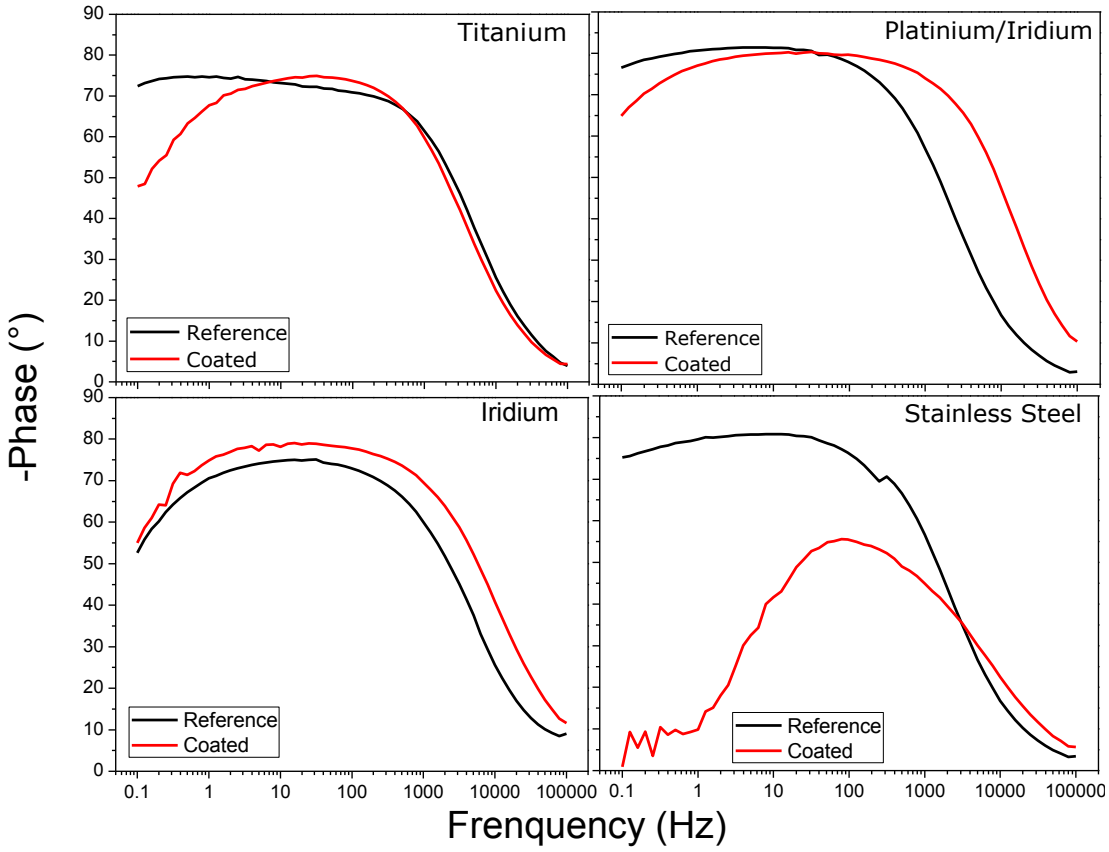

Figure 24: EIS Bode plots of the phase of uncoated reference and coated electrodes in PBS electrolyte solution; Ti (L11018O), Ir (L11020D), Pl/Ir(L11020G), SS(L11018M)

Stainless steel as a substrate for coated electrodes initially shows similar behavior as previously mentioned substrates. In the higher frequency ranges an upward shift of the coated electrode graph is visible. When the frequency drops below 1kHz the slope of the graph begins to gradually decrease. This behavior however is not seen in the uncoated electrode which indicates that the coated electrode has a technical malfunction possible due to construction from coated wire substate.

In figure 24 the Bode plots of the phase for all four substrate types are shown with the negative phase shift in function of frequency. The substrates Iridium and Platinum/Iridium show a similar result compared to their respective reference graphs, namely a shift to the right and possibly also an upward shift for the coated Iridium electrode. The rightward shift of the graph indicates a decreasing interface capacitance which suggests the previously mentioned observations of the modulus plots that the contact area of electrode-electrolyte interface has decreased due to thin film coating.
The coated titanium electrode shows partial overlap with the uncoated reference graph in the higher frequency range but gradually decrease further while the reference graph stays constant in the lower frequency range. This indicates that at the electrode-electrolyte interface of an uncoated titanium electrode charge transfer takes place (, possibly due to oxidation of the titanium) and that coating of the surface blocks this process.
For stainless steel an initial rightward shift is seen in the graph of the coated electrode but below 4kHz the graph gradually decreases and the signal starts to oscillate randomly. This also indicates that the coated electrode has a possible technical malfunction

3.4.2 Cyclic Voltammetry of NCD Coated Electrodes

Functional analysis of coated electrodes through cyclic voltammetry is done in PBS and 10 mM potassium ferricyanide as electrolyte solution. Every coated electrode is analyzed and compared to an uncoated reference electrode of the same material. Subsequently the tip of the electrode is dipped in PDMS to nullify the effects of partial or no coating at the tip of the wire as seen by SEM results. Below are the results listed which register a significant change in behavior while the rest is found in the appendix (Appendix fig.13-15)

The cyclic voltammograms of the titanium electrodes seen in figure 25 show that coating has a clear effect on electrode behavior. The peak registered by the uncoated reference electrode at -0,85V disappears when the electrode is coated. It indicates that a irreversible redox reaction is blocked by the coating.

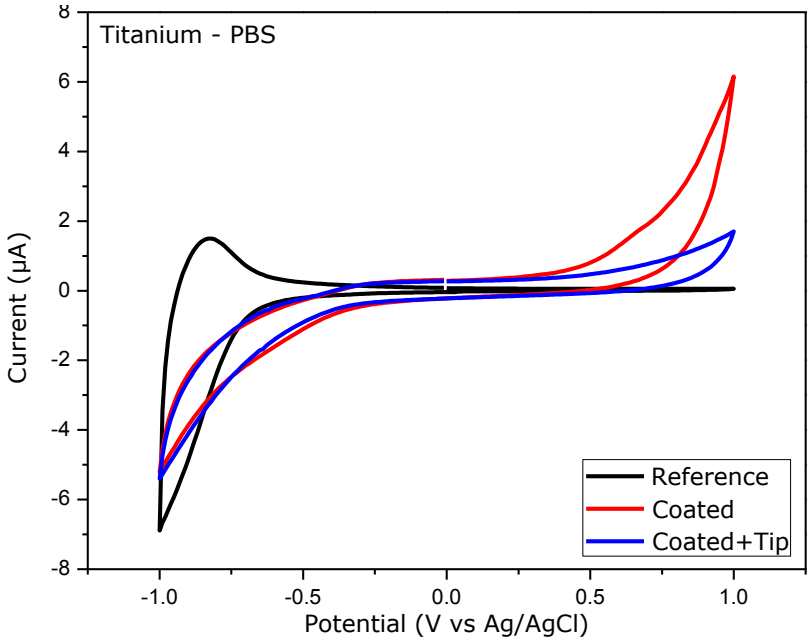

Figure 25: Cyclic Voltammogram Ti electrode (L11018O) in PBS

The cyclic voltammograms of the iridium electrodes in PBS are depicted in figure 26 and all show a high degree of overlap with the exception the downward peak at -1V. As the applied potential decreases further below -0,75 a current starts to flow drastically. Coating of the electrode however has a partially inhibiting effect on this electrode behavior. Covering the insufficiently coated tip of the electrode with PDMS further inhibits this.

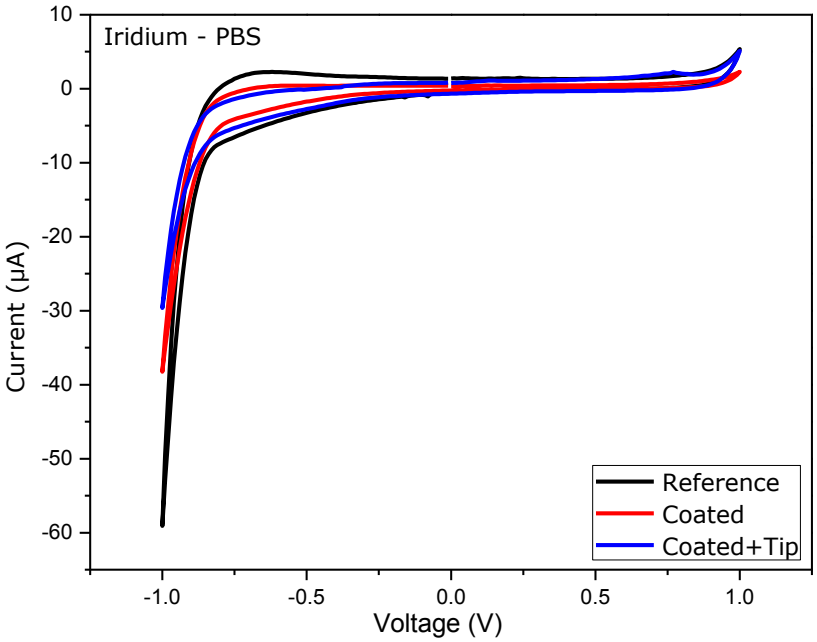

Figure 26: Cyclic Voltammogram Ir electrode (L11020D) in PBS

The cyclic voltammograms of the platinum/iridium electrodes in PBS are seen in figure 27. When the uncoated reference and coated electrode are compared two changes are observed in the behavior of the electrode. Firstly the upward peak at 0,7V is no longer

present indicating a irreversible redox reaction is stopped by coating the Pl/Ir electrode with a thin film. Secondly, the current which starts to flow below -0,6V and rapidly increases when the applied negative potential increases further is profoundly inhibited by the presence of a thin film coating. Covering of the tip of the electrode with PDMS does not further improve this effect indicating a large portion of the surface is indeed coated with a thin film as SEM results (fig.22) suggest.

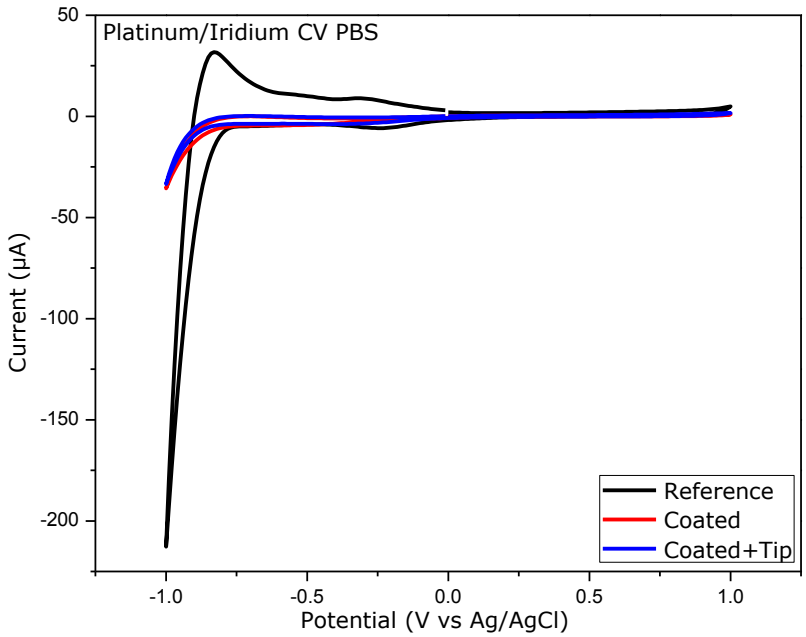

Figure 27: Cyclic Voltammogram Pl/Ir electrode (L11020G) in PBS

Depicted in figure 28 are the cyclic voltammograms of Pl/Ir electrodes measured in potassium ferricyanide. When comparing the coated electrode to the uncoated reference electrode, changes are observed in electrode behavior after coating. The increasingly large current flowing when the negative potential is increased is partially inhibited. Also the reversible redox reaction taking place at the electrode-electrolyte interface is inhibited as well. This is seen by the lowering of the redox peaks at 0,1V and 0,3V which give the characteristic shape to the voltammogram when such a redox reaction is present. When comparing the coated electrode after covering the tip with DPMS both effects are enhanced even further. The reversible redox reaction is blocked completely and the current flowing when a negative potential of -1V is applied is reduced to almost zero. This not only shows a as good as complete coverage of the electrode which is supported by SEM results (fig.21,22) but also shows that no electrical currents can flow and therefore charge transport is highly limited. This electrode materials suits for capacitive applications such as sensing or pacing potential.

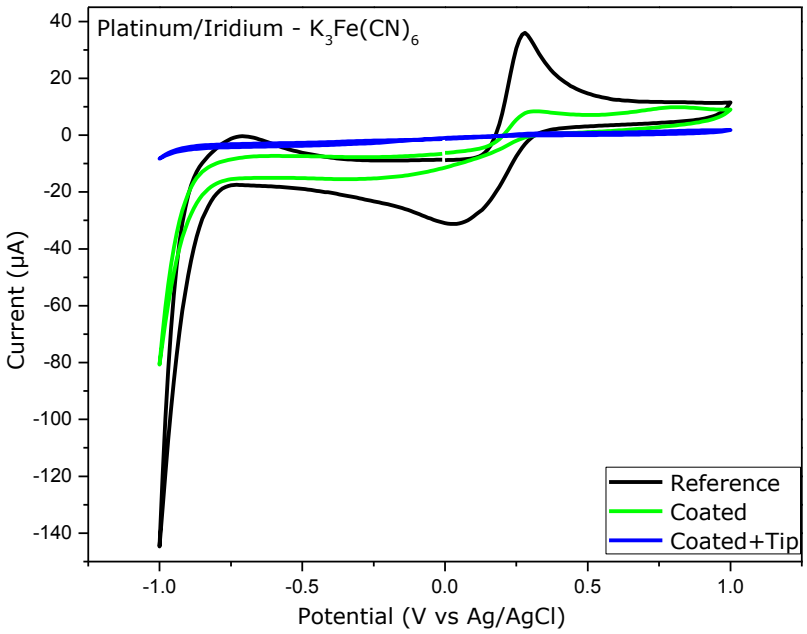

Figure 28: Cyclic Voltammogram Pl/Ir electrode (L11020G) in $K_3Fe(CN)_6$

The cyclic voltammograms of the stainless steel electrodes measured in 10 mM potassium ferricyanide and PBS solution are shown in Appendix figure 15-16. In both experiments the reference electrode registers a stable voltrammogram after 2 cycles of the voltage sweep range. The coated electrode however registers a gradually increasing current after each completed cycle. Similar to EIS analysis this is an indication that the electrode suffers from a technical malfunction probably due to fouling or loss of proper electrode function.

The combined results of EIS and CV show that coating the surface of an electrode with NCD can have beneficial effects without drastically changing the functionality of the electrode. Charge transfer reactions have been blocked in coated titanium and platinum/iridium electrodes. Strongly growing currents when an increased negative potential is applied are seen to be partially or largely inhibited when titanium, iridium and platinum/iridium electrodes are coated. These changes in the behavior of the electrodes should not be detrimental to the functionality of a pacemaker electrode as this device induces pulse transfer to tissue by changes in the surround electric fields. The Bode plots of iridium, platinum/iridium and possibly titanium indicate a impedance increase as well as a phase shift to higher frequencies. The increase in impedance is due to the NCD being undoped and thus poorly conducting. The frequency shift to the right indicates the contact area of electrode-electrolyte is decreasing because of the thin film coating. Again these effects should not necessarily have a negative impact as charge transfer across the electrode-electrolyte interface is not the pulse transfer mechanism of the a cardiac assisting device. The presence of the thin film does however change the makeup of the electrode-electrolyte interface itself. The top electrode layer in contact with the

electrolyte is now made of nanocrystalline diamond stead of metal. This could influence the processes taking place at the electrode-electrolyte interface because the surface on which the Helmholtz double layer forms has changed. To what degree these influences extend should be further investigated.

4 Conclusion

Thin film deposition of NCD diamond is attempted on metals relevant to cardiac stimulating electrodes. Metal wires made of titanium, iridium, platinum/iridium and stainless steel are used as substrate. Instead of genuine cardiac electrodes, wires of the material and cylindrical shape are used to verify proof-of-principle. During fine tuning of substrate pretreatment three different techniques of seeding in solution were tested. Raman spectroscopy was used to determine the effectiveness of each technique. As the time for each thin film deposition in the CVD reactor is set to 6 hours no diamond is able to form through spontaneous nucleation. Only if the substrate surface is successfully covered with a monolayer of nanodiamonds will a diamond raman peak be registered at 1332,45 cm^{-1}. Of all three techniques only diamond was detected when the substrate was sweeped with a droplet of seeding solution at the tip of a pipette while standard dip coating and seeding in a ultrasonicated bath were revealed to be ineffective. Because the diameter of the substrate wires are in the sub-millimetre microfluidic effects interfered which made seeding troublesome.

After thin films were coated on substrate wires of Ti, Ir, Pl/Ir and SS optical characterization was done using raman spectroscopy. The spectral results show all thin films are composed of diamond and different forms of sp^2-carbon. This suggest the thin films to be of NCD nature and proofs coating of cylindrical shaped metal substrates is possible. Spectra taken from different positions along the surface of the each substrate type show similar peak patterns indicating thin film composition is homogeneous throughout the film. Coatings on stainless steel also exhibited minor internal stresses as the diamond peaks of the SS spectra are shifted several wavenumbers. This is probably caused by the different lattice constants of the metals incorporated in stainless steel alloy. Peak fitting of the individual spectra estimated the diamond-to-graphite ratio of the films on all substrate types to lie between 74,38% and 82,72% which is consistent with the fact that all thin films were grown under the same CVD conditions. The values for full with at half maximum of the diamond peaks lie between 38,65 cm^{-1} and 30,95 cm^{-1} what is an acceptable range for nanocrystalline diamond according to literature. The values calculated with the peak fitting procedure should however be seen as a rough estimate as the limitations of the used software make it prone to incorporate errors.

To investigate the morphology of the thin film coatings scanning electron microscopy was used. The results indicate that a thin film coating is indeed present on all substrate types. However the typical surface pattern of NCD is only vaguely recognizable. Without the results from raman spectroscopy classification of the thin film would have been inconclusive. The pattern of the film's surface could have been the result of the surface defects of the underlying substrate which are known by atomic force microscopy to be

relatively rough. The structural integrity of the films varies according to the location on the wire substrate. Spots exhibiting continuous thin film coating are found more along the shaft of the wire then at the tip. The main reason being the problematic seeding at the tip due to microfluidic effects and the other being the strong deformation of the substrate surface when wire was cut with pliers. There are also marks of film delamination on locations at the tip of the wire.

To investigate the functionality of NCD coated electrodes EIS and CV were done in a custom built electrochemical cell. NCD coated electrodes were constructed using coated wires. The results show the surface of a metal electrode can be coated with NCD without drastically changing the functionality of the electrode. The coating is able to able to block charge transfer reactions while also inhibiting the strongly growing currents when an increasing negative potential is applied to the electrode. It was also report that the impedance of the electrode-electrolyte interface is increased after coating which is consistent with the undoped nature of the NCD film. These changes in the behaviour of the electrode however should not necessarily have a negative influence on the functionality of a pacing electrode as pulse transfer to tissue occurs through changes in electric fields. The presence of the thin film does however change one component of the electrode-electrolyte interface. The surface layer of the electrode which is in contact with the electrolyte is now made of NCD instead of metal. This could influence the processes taking place at the electrode-electrolyte interface because the surface on which the Helmholtz double layer forms has changed along with its intrinsic properties.

To conclude, the coating of nanocrystalline diamond on materials relevant to cardiac stimulating electrodes as well as the functionality of these electrodes is confirmed in principle. Of the substrates used titanium showed superior film morphology due to facilitated seeding by the strongly hydrophilic character of the substrate's surface. Based on electrode functionality platinum/iridium is the most promising substrate to continue research. The aspect that needs most improving is the quality of the thin film. Using larger substrates such as genuine cardiac electrodes should facilitate the seeding procedure which directly promotes formation of a continuous film. Also the CVD growth conditions can be fine tuned to better suite each type of substrate. This will result in a better film adhesion and a higher diamond-to-graphite ratio. When above mentioned thin film conditions meet a sufficiently high standard on a genuine cardiac electrode in vivo experiments can follow to investigate the consequences of the changed electrode-electrolyte interface.

5 References

1. Ratner B, Hoffman AS, Schoen FJ, Lemons JE. Biomaterials science: a multidisciplinary endeavor. In: Ratner B, Hoffman AS, Schoen FJ, Lemons JE, editors. Biomaterials science, an introduction to materials in medicine. 2nd edition. California/London: Elsevier Academic Press; 2004. p. 1-9

2. Ellenbogen KA, Kay G, Lau GN. Basic principles of device therapy. In: Ellenbogen KA, Kay G, Lau GN, editors. Clinical cardiac pacing, defibrillation, and resynchronization therapy. 3rd edition. Philiadelphia: Saunders Elsevier; 2007. p. 1-2

3. Ellenbogen KA, Kay G, Lau GN. Engineering and construction of pacemaker and implantable cardioverter-defibrillator leads. In: Ellenbogen KA, Kay G, Lau GN, editors. Clinical cardiac pacing, defibrillation, and resynchronization therapy. 3rd edition. Philiadelphia: Saunders Elsevier; 2007. p. 161-200

4. Image of implanted dual chamber pacemaker [Image on the internet] Available from: http://www.drugs.com/cg/pacemaker-precare.html

6. Perry L, Karp F, Hauch K, Ratner BD. Explanted pacemakers: observations of the long-term foreign body respons. JURIBE 2007.

5. Anderson JM, Rodriguez A, Chang DT. Foreign body reaction to biomaterialsSemin Immunol 2008 apr;20(2):86-100

7. Mani G, Feldman MD, Patel D, Agrawel CM. Coronary stents: a materials perspective. Biomaterials 2007;28:1689-1710

8. Eisenbarth E, Velten D, Müller M, Thull R, Breme J. Biocompatibility of β-stabilizing elements of titanium alloys. Biomaterials 2004;25:5705-5713

9. Motohiro U, Watari F, Yokojama A, Matsuno H, Kawasaki T. Tissue reaction around metal implants observed by X-ray Scanning Analytical Microscopy. Biomaterials 2001;22:377-685

10. Mitura K, Niedzielski P, Bartosz G, Moll J, Walkowiak B, Pawlowska Z, Louda P, Kiec-Swierczynska M, Mitura S. Interactions between carbon coatings and tissue. Surf Coat Tech 2006;201:2117-2123

11. Tang L, Tsai C, Gerberich WW, Kruckeberg L, Kania DR. Biocompatibility of chemical-vapour-deposited diamond. Biomaterials 1995;16:483-488

12. Jakubowski W, Bartosz G, Niedzielski P, Szymanski W, Walkowiak B. Nanocrystalline diamond surface is resistant to bacterial colonization. Diam and Rel Mat 2004;13:1761-1763

13. Okroj W, Kaminska M, Klimek L, Szymanski W, Walkowiak B. Blood platelets in contact with nanocrystalline diamond surfaces. Diam and Rel Mat 2006;15:1535-1539

14. Nurdin N, François P, Mugnier Y, Krumeich J, Moret M, Aronsson BO, Descouts P. Haemocompatibility evaluation of DLC- and SIC-coated surfaces. Euro Cell and Mat 2003;5:17-28

15. Huang H, Pierstorff E, Oawa E, Ho D. Protein-mediated Assembly of Nanodiamond Hydrogels into a Biocompatible and Biofunctional Multilayer Nanofilm. ACS Nano 2008;2:203-212

16. Hui YY, Cheng CL, Chang HC. Nanodiamonds for optical Bioimaging. Jour Phys D 2010;43:374021

17. Papo MJ, Catledge SA, Vohra YK, Machado C. Mechanical Wear Behavior of Nanocrystalline and Multilayer Diamond Coatings on Tempormandibular Joint Implants. J Mater Sci: Mater M 2004;15:773-777

18. Jozwik K, Karczemska A. The New Generation Ti6Al4V Artificial Heart Valve with Nanocrystalline diamond Coating on the T-Ring and with Derlin Disc after Long-term Mechanical Fatigue Examination. Diam Relat Mater 2007;16:1004-1009

19. Koizumi S, Nebel CE, Nesladek M. Growth and properties of nanocrystalline diamond films. In: Koizumi S, Nebel CE, Nesladek M, editors. Physics and applications of cvd diamond. Weinheim, Wiley-VCH: 2007; p. 13-28

20. Krueger A. Diamond films. In: Krueger A, editor. Carbon materials and nanotechnology. Weinheim, Wiley-VCH: 2010; p. 389-451

21. Ellenbogen KA, Kay G, Lau GN. Cardiac electrical stimulation. In: Ellenbogen KA, Kay G, Lau GN, editors. Clinical cardiac pacing, defibrillation, and resynchronization therapy. 3rd edition. Philiadelphia: Saunders Elsevier; 2007. p. 3-59

22. Narayan RJ, Boehm RD, Sumant AV. Medical Applications of Diamond Particles & Surfaces. Mat To;14:154-163

23. Krueger A. Diamond films. In: Krueger A, editor. Carbon materials and nanotechnology. Weinheim, Wiley-VCH: 2010; p. 389-451

24. Yan B, Loh NL, Fu Y, Sun CQ, Hing P. Surface and interface characterization of diamond coatings deposited on pure titanium. Surf Coat Tech 1999;115:256-265

25. Tsubota T, Ohta M, Kusakabe K, Morooka S, Watanabe M, Maeda H. Heteroepitaxial growth of diamond on an iridium (100) substrate using microwave plasma-assisted chemical vapor deposition. Diam and Rel Mat 2000;9:1380-1387

26. Tachibana T, Yokota Y, Miyata K, Kobashi K, Shintani Y. Heteroepitaxial diamond growth process on platinum (111). Diam and Rel Mat 1997;6:266-271

27. Morrison NA, Drummond IC, Garth C, John P, Milne DK, Smith GP, Jubber MG, Wilson JIB. Growth of CVD diamond films over bio-medical materials. Diam and Rel Mat 1996;5:1118-1126

28. SEM image of clustered diamond nanoparticles [Image on the internet] Available from: http://thediamondgeyser.blogspot.com/2008/10/detonation-nano-diamond-paper.html

29. Mendes de Barros RC, Corat EJ, Fereira NG, de Souza TM, Trava-Airoldi VJ, Leite NF, Iha K. Dispersion liquid properties for efficient seeding in CVD diamond nucleation enhancement. Diam and Rel Mat 1996;5:1323-1332

30. Taylor A, Fendrych F, Fekete L, Vlcek J, Rezacova V, Petrak V, Krucky J, Nesladek M, Liehr M. Novel high frequency pulsed MW-linear antenna plasma-chemistry: Routes towards large area, low pressure nanodiamond growth. Diam and Rel Mat 2011;20:613-615

31. Liehr M, Dieguez-Campo M. Microwave PECVD for large area coating. Surf and Coat Tech 2005;200:21-25

32. Krueger A. Diamond films. In: Krueger A, editor. Carbon materials and nanotechnology. Weinheim, Wiley-VCH: 2010; p. 389-451

33. Zhang Q, Li HD, Cheng, SH, Wang QL, Li LA, Lv XY, Zou GT. The effect of CO_2 on the high-rate homoepitaxial growth of CVD single crystal diamonds. Diam and Rel Mat 2011;20:496-500

34. Schematic explaining principles of Raman spectroscopy. [Image on the internet] Available from: http://newton.ex.ac.uk/research/biomedical-old/optics/sers.html

35. Fortunato W, Chiquito AJ, Galzerani JC, Moro JR. Crystalline quality and phase purity of CVD diamond films studied by Raman spectroscopy. J Mater Sci 2007;42:7331-7336

36. Fortunato W, Chiquito AJ, Galzerani JC, Moro JR. Crystalline quality and phase purity of CVD diamond films studied by Raman spectroscopy. J Mater Sci 2007 [cited 2007];42:7333

37. Fortunato W, Chiquito AJ, Galzerani JC, Moro JR. Crystalline quality and phase purity of CVD diamond films studied by Raman spectroscopy. J Mater Sci 2007 [cited 2007];42:7331

38. Schematic explaining principles of AFM. [Image on the internet] Available from: http://www.farmfak.uu.se/farm/farmfyskem-web/instrumentation/afm.shtml

39. Schematic explaining principles of SEM. [Image on the internet] Available from: http://www.purdue.edu/rem/rs/sem.htm

40. Katz E, Willner I. Probing Biomolecular Interactions at Conductive and Semiconductive Surfaces by Impedance Spectroscopy: Routes to Impedimetric Immunosensors, DNA-Sensors, and Enzyme Biosensors. Electroanalysis 2003;15:913-947

41. Katz E, Willner I. Probing Biomolecular Interactions at Conductive and Semiconductive Surfaces by Impedance Spectroscopy: Routes to Impedimetric Immunosensors, DNA-Sensors, and Enzyme Biosensors. Electroanalysis 2003;15:913-947

42. Wang J. Cyclic Voltammetry. In: Wang J, editor. Analytical Electrochemistry. London, John Wiley & Sons 2000;2:25-37

Appendix

Appendix table 1: Properties and specifications of metal wires

Substrate	Diameter (mm)	Purity (%)	Melting Temp. (°C)	Elect. Res. (μ.Ω.cm)	Ther. Exp. Coëf. (μm/m.K)
Titanium	0.250	99.99	1660	54.0	8.9
Iridium	0.250	99.90	2410	5.1	16.0
Platinum/ Iridium 90/10	0.250	/	1770	10.6	6.8
Stainless Steel	0.358	/	1510	74.0	9.0

Appendix table 2: CVD growth conditions of each run

Run code	Gas flow ratio (sccm)			Time (h)	Pressure (mBar)	Temp. subst. (°C)	Pulse Power (W)	Pulse Freq. (Hz)	Average Power (W)	
	H_2	CH_4	CO_2						Forward	Reflected
L11011	460	25	25	10:30	1.002	450-500	8000	4545	2450	340
L11012	690	37.5	22.5	8:55	1.001	<450	8000	4545	2450	350
L11013	740	40.25	24.15	0:25	1.001	<450	8000	4545	2450	340
	40.25	12.5	7.5	6:35	1.001	<450	7500	4545	2450	340
L11014	460	25	15	7:00	1.001	<450	8000	4545	2480	475
L11016	690	37.5	22.5	6:10	1.002	<450	8000	4545	2460	380
L11017	460	25	15	6:00	1.001	450	8000	4545	2450	350
L11018	460	25	15	6:00	1.001	450-500	8000	4545	2340	400
L11020	460	25	15	6:00	1.001	450-500	8000	4545	2480	500
L11025	460	25	15	6:00	1.001	450-500	8000	4545	2460	480

Appendix table 3: List of substrates

Sample	Substrate
L11011-A	Titanium
L11011-B	Titanium
L11012-A	Titanium
L11012-B	Titanium
L11013-A	Titanium
L11013-B	Iridium
L11013-C	Platinum/Iridium
L11014-A	Titanium
L11014-B	Titanium
L11014-C	Stainless Steel
L11014-D	Stainless Steel
L11016-E	Titanium
L11016-F	Stainless Steel
L11016-G	Titanium
L11017-G	Stainless Steel
L11017-H	Stainless Steel
L11017-I	Stainless Steel
L11017-J	Stainless Steel
L11018-L	Stainless Steel
L11018-M	Stainless Steel
L11018-N	Titanium
L11018-O	Titanium
L11020-D	Iridium
L11020-E	Iridium
L11020-F	Platinum/Iridium
L11020-G	Platinum/Iridium
L11025-H	Titanium
L11025-I	Titanium
L11025-J	Iridium
L11025-K	Iridium

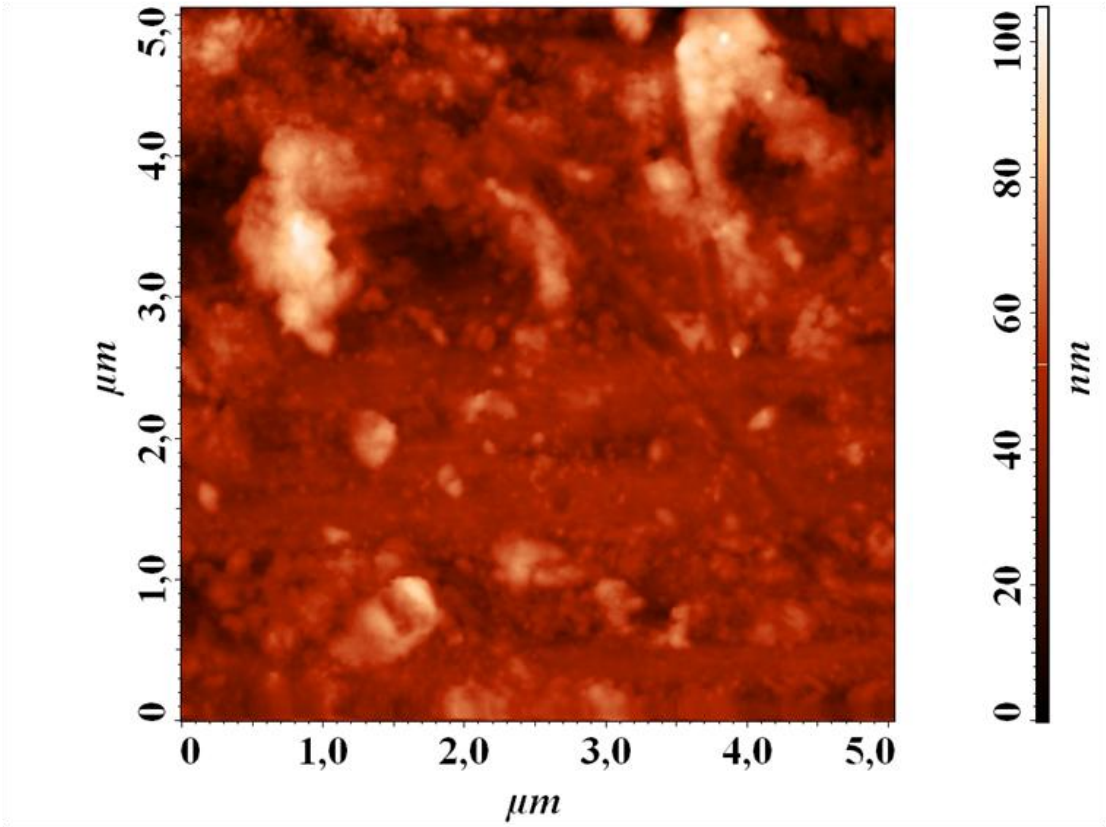

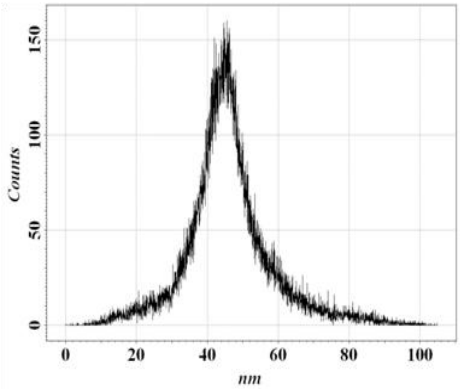

Amount of sampling	65536
Max	104,904 nm
Min	0 nm
Peak-to-peak, Sy	104,904 nm
Ten point height, Sz	52,6319 nm
Average	46,0749 nm
Average Roughness, Sa	8,56318 nm
Second moment	47,644
Root Mean Square, Sq	**12,1268 nm**
Surface skewness, Ssk	0,603804
Coefficient of kurtosis, Ska	2,06954
Entropy	10,1849
Redundance	-0,520344

Appendix figure 1: AFM results cleaned SS wire

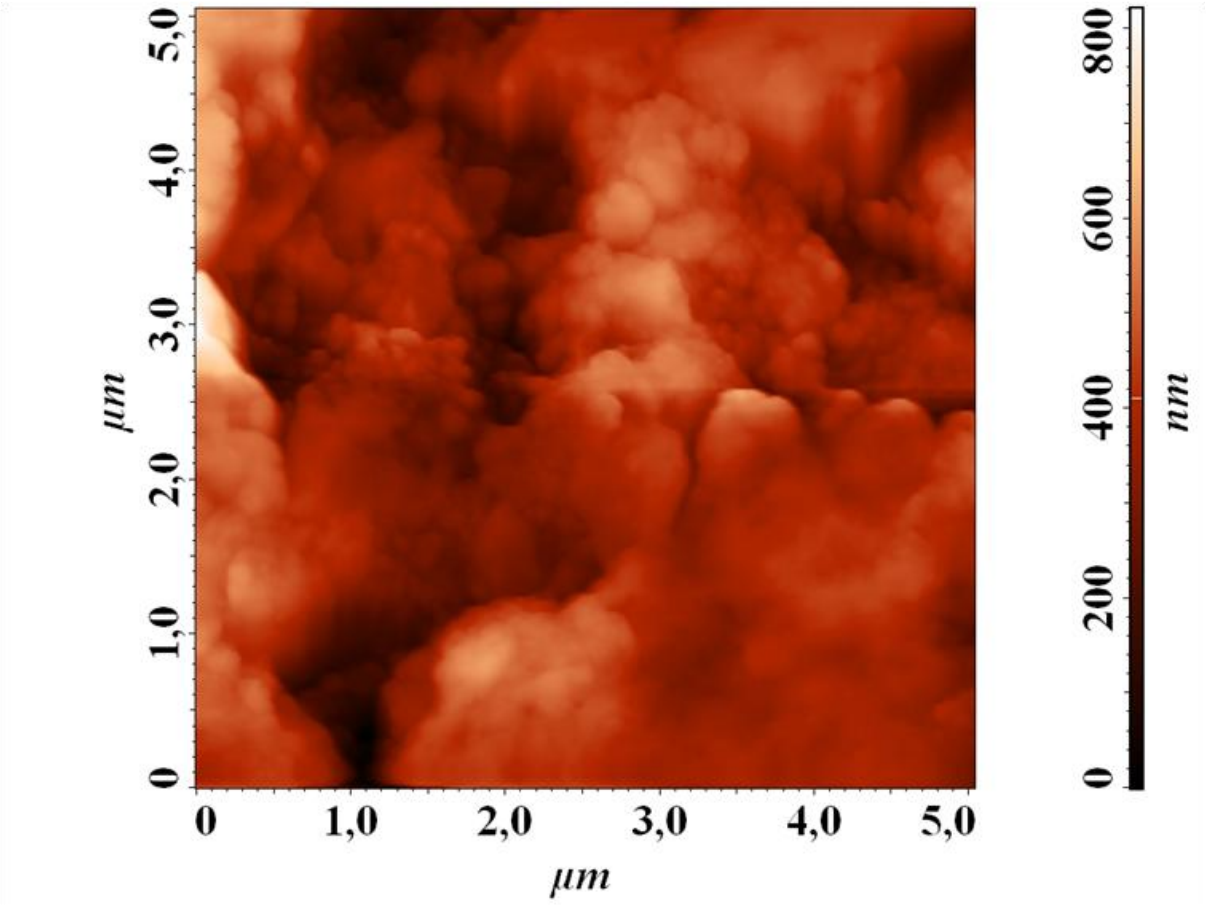

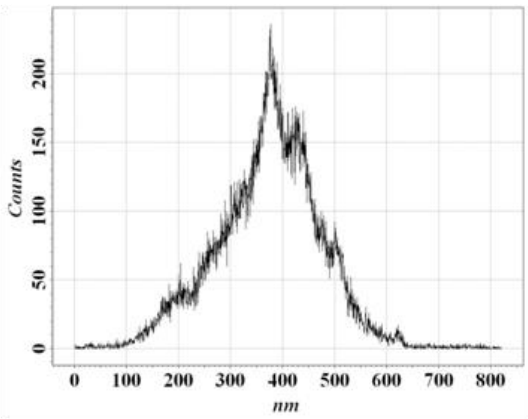

Amount of sampling	65536
Max	820,309 nm
Min	0 nm
Peak-to-peak, Sy	820,309 nm
Ten point height, Sz	408,45 nm
Average	373,922 nm
Average Roughness, Sa	77,1082 nm
Second moment	387,063
Root Mean Square, Sq	**99,9974 nm**
Surface skewness, Ssk	-0,116605
Coefficient of kurtosis, Ska	0,591926
Entropy	13,1679
Redundance	-0,360564

Appendix figure 2: AFM results cleaned Ti wire

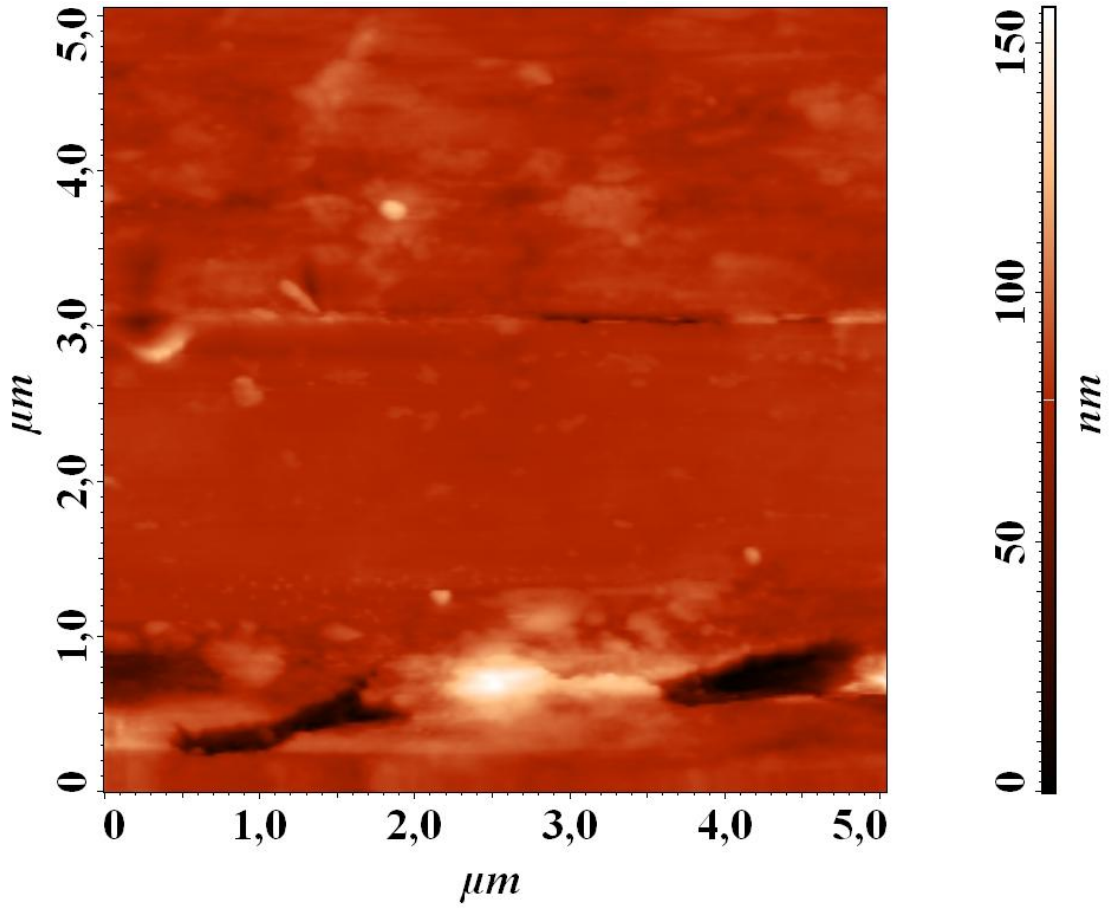

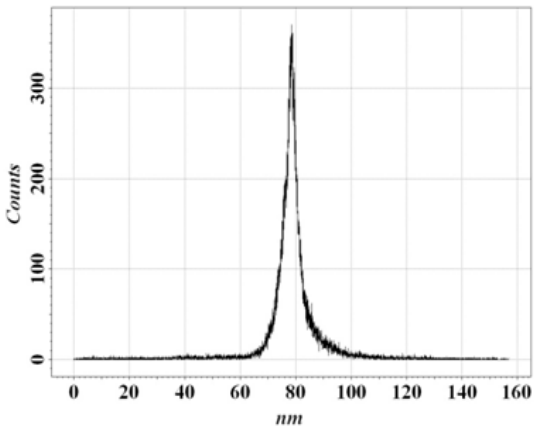

Amount of sampling	65536
Max	156,838 nm
Min	0 nm
Peak-to-peak, Sy	156,838 nm
Ten point height, Sz	78,358 nm
Average	78,8214 nm
Average Roughness, Sa	5,684 nm
Second moment	79,6213
Root Mean Square, Sq	**11,2581 nm**
Surface skewness, Ssk	-0,646444
Coefficient of kurtosis, Ska	14,7516
Entropy	9,37363
Redundance	-0,286895

Appendix figure 3: AFM results cleaned Ir wire

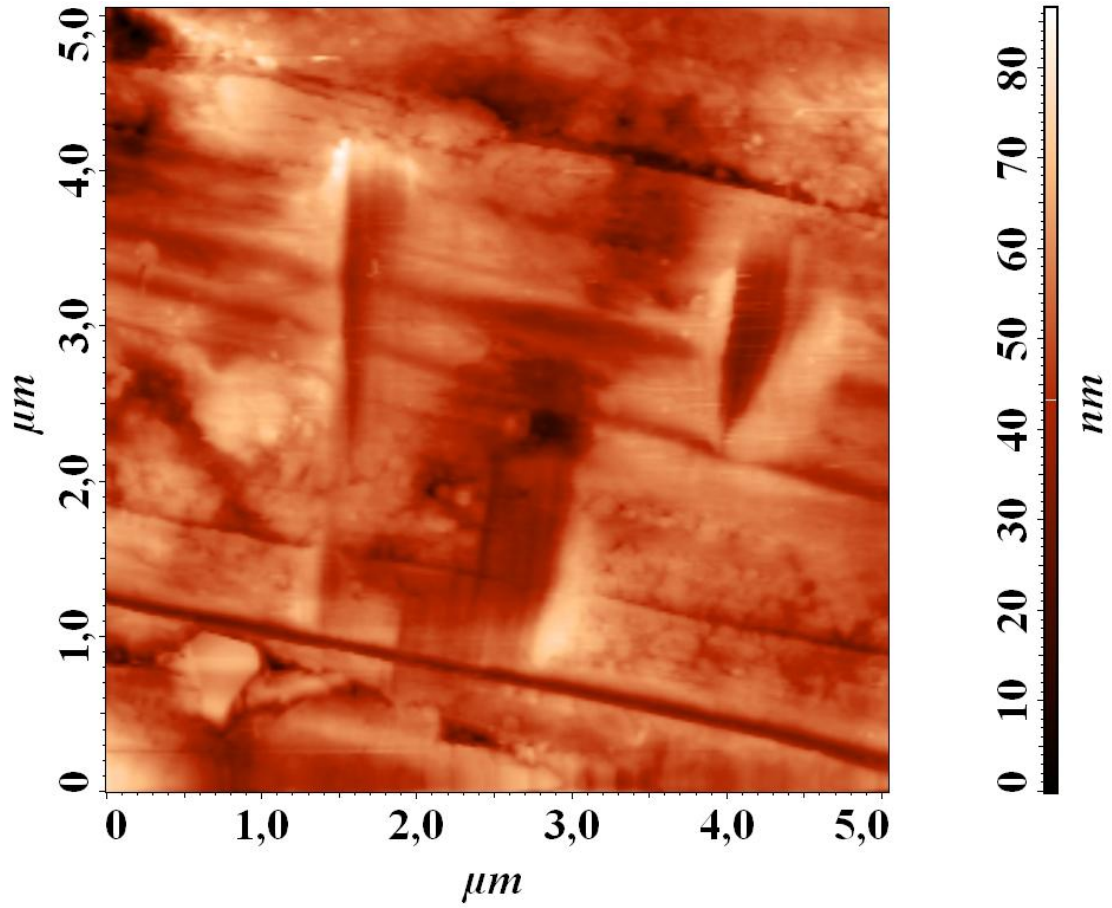

Amount of sampling	65536
Max	86,4814 nm
Min	0 nm
Peak-to-peak, Sy	86,4814 nm
Ten point height, Sz	42,9803 nm
Average	49,8667 nm
Average Roughness, Sa	7,40867 nm
Second moment	50,7611
Root Mean Square, Sq	**9,4874 nm**
Surface skewness, Ssk	-0,41629
Coefficient of kurtosis, Ska	0,627362
Entropy	9,94552
Redundance	-0,549741

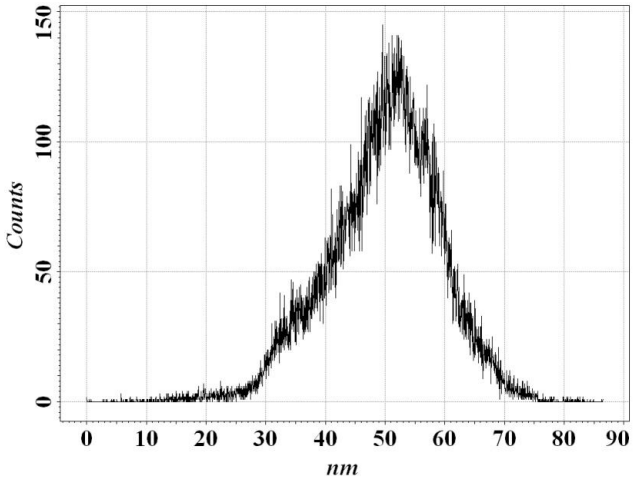

Appendix figure 4: AFM results cleaned Pl/Ir wire

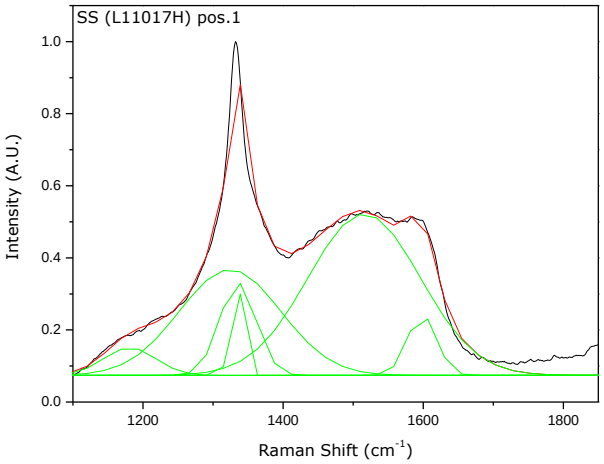

Data: H17_B
Model: Gauss
Equation: y=y0 + (A/(w*sqrt(PI/2)))*exp(-2*((x-xc)/w)^2)
Weighting:
y No weighting

Chi^2/DoF = 0.00296
R^2 = 0.9279

y0	0.07394	±0.00236
xc1	1181.15803	±24.09398
w1	73.95072	±39.6592
A1	7.13476	±12.07993
xc2	1335.54361	±2.52931
w2	51.76981	±16.04608
A2	16.71249	±12.20281
xc3	1332.15994	±0.63781
w3	15.07708	±1.96065
A3	6.51374	±1.50632
xc4	1324.24106	±9.74849
w4	144.88727	±95.1369
A4	53.32118	±18.01497
xc5	1515.77631	±17.94889
w5	160.1934	±15.529
A5	89.8818	±16.30341
xc6	1598.36121	±2.16313
w6	41.39424	±5.76556
A6	8.7461	±1.90684

Appendix figure 5:Peak fitting raman spectrum SS (L11017H) position 1

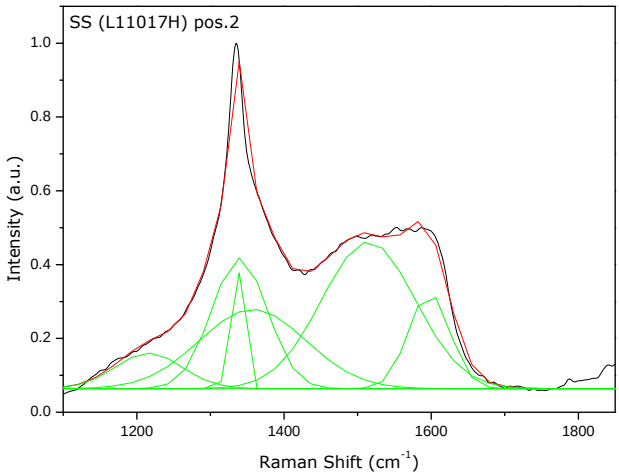

Data: H17_C
Model: Gauss
Equation: y=y0 + (A/(w*sqrt(PI/2)))*exp(-2*((x-xc)/w)^2)
Weighting:
y No weighting

Chi^2/DoF = 0.00122
R^2 = 0.96903

y0	0.06399	±0.00149
xc1	1216.16463	±43.42094
w1	90.84573	±39.12289
A1	10.97059	±20.18873
xc2	1339.61079	±7.66514
w2	75.49744	±29.16805
A2	33.50229	±61.21154
xc3	1334.63384	±0.39212
w3	16.41418	±1.10778
A3	7.47785	±0.79457
xc4	1357.57441	±126.12271
w4	144.60657	±282.18013
A4	38.98221	±45.6639
xc5	1514.86061	±42.1778
w5	127.03939	±24.07117
A5	63.37224	±45.25853
xc6	1597.43111	±2.01741
w6	55.86218	±5.179
A6	18.21684	±4.34906

Appendix figure 6:Peak fitting raman spectrum SS (L11017H) position 2

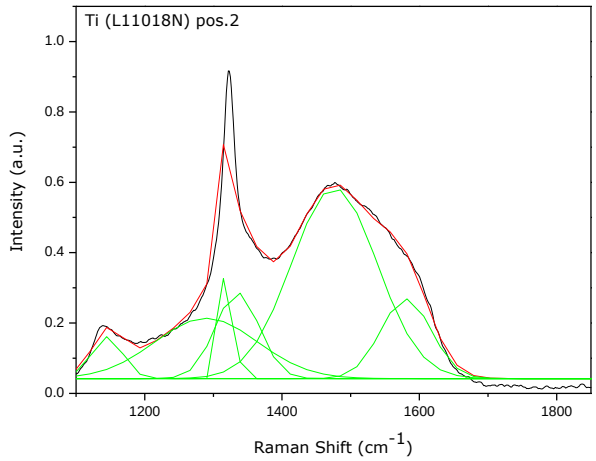

Data: N18_C
Model: Gauss
Equation: y=y0 + (A/(w*sqrt(PI/2)))*exp(-2*((x-xc)/w)^2)
Weighting:
y No weighting

Chi^2/DoF = 0.00672
R^2 = 0.84597

y0	0.04209	±0.00344
xc1	1145.3625	±4.90259
w1	44.90049	±15.20076
A1	6.72713	±4.13096
xc2	1334.94738	±7.24631
w2	63.53768	±29.54048
A2	19.50569	±32.33003
xc3	1322.24398	±0.73978
w3	15.73667	±1.89192
A3	8.94324	±1.56605
xc4	1289.62035	±187.00637
w4	149.76019	±201.97921
A4	32.18704	±80.93566
xc5	1476.13368	±18.81919
w5	124.54358	±71.21156
A5	84.52137	±67.8606
xc6	1580.61221	±12.87833
w6	73.44607	±22.19779
A6	20.89005	±24.19925

Appendix figure 7:Peak fitting raman spectrum Ti (L11018N) position 2

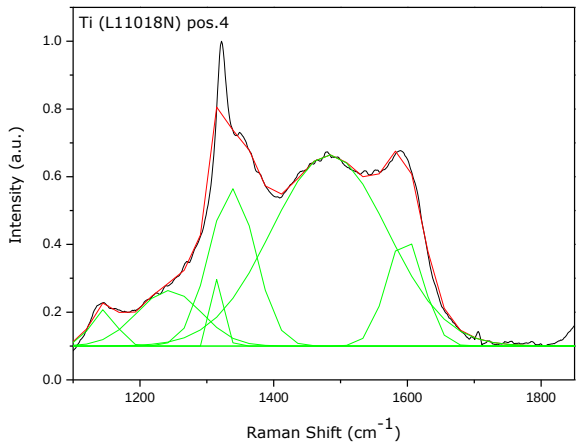

Data: N18_E
Model: Gauss
Equation: y=y0 + (A/(w*sqrt(PI/2)))*exp(-2*((x-xc)/w)^2)
Weighting:
y No weighting

Chi^2/DoF = 0.00405
R^2 = 0.92784

y0	0.10008	±0.00274
xc1	1145.45944	±4.59988
w1	37.99501	±10.59095
A1	5.11176	±2.36369
xc2	1243.71341	±21.0763
w2	95.75088	±47.78453
A2	19.63172	±10.87252
xc3	1321.401	±0.6651
w3	13.14552	±1.66044
A3	5.4888	±0.90318
xc4	1337.95305	±5.80589
w4	68.88557	±7.29237
A4	40.12895	±10.72596
xc5	1483.30844	±3.73405
w5	173.2365	±9.05048
A5	122.54418	±6.31814
xc6	1596.35581	±1.47973
w6	54.5065	±4.36159
A6	22.00603	±2.94935

Appendix figure 8:Peak fitting raman spectrum Ti (L11018N) position 4

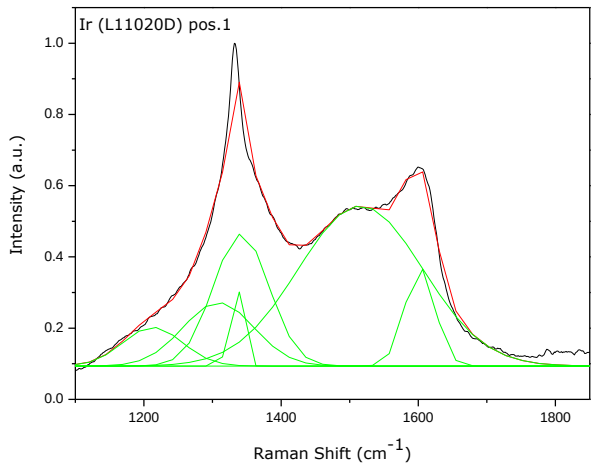

Data: D20_B
Model: Gauss
Equation: y=y0 + (A/(w*sqrt(PI/2)))*exp(-2*((x-xc)/w)^2)
Weighting:
y No weighting

Chi^2/DoF = 0.00127
R^2 = 0.97114

y0	0.0937	±0.00157
xc1	1212.89081	±155.21842
w1	86.3164	±78.41563
A1	11.79694	±73.72133
xc2	1308.64173	±627.79627
w2	103.64776	±288.56879
A2	23.13775	±302.69105
xc3	1332.02437	±0.45859
w3	15.54594	±1.22083
A3	6.01785	±0.69969
xc4	1341.76095	±76.34559
w4	81.04426	±84.03106
A4	37.70851	±368.46654
xc5	1515.80277	±5.68688
w5	181.27936	±6.62756
A5	102.15062	±4.01525
xc6	1602.49356	±0.88084
w6	43.95241	±2.27316
A6	15.19998	±1.15097

Appendix figure 9:Peak fitting raman spectrum Ir (L11020D) position 1

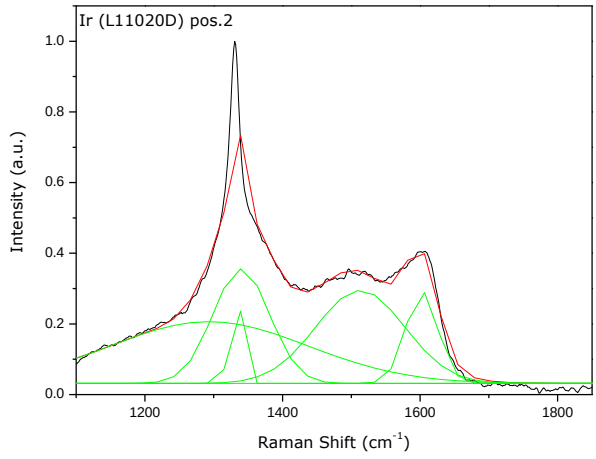

Data: D20_C
Model: Gauss
Equation: y=y0 + (A/(w*sqrt(PI/2)))*exp(-2*((x-xc)/w)^2)
Weighting:
y No weighting

Chi^2/DoF = 0.00124
R^2 = 0.95728

y0	0.03158	±0.00191
xc1	1293.33227	±47.52293
w1	288.22668	±44.9888
A1	63.13961	±19.9449
xc2	1330.13363	±0.26851
w2	13.96225	±0.65479
A2	7.94762	±0.45297
xc3	1339.97084	±1.46641
w3	82.32088	±5.28645
A3	33.49012	±5.47842
xc4	1512.94308	±5.22759
w4	129.73412	±18.97073
A4	42.80812	±14.58846
xc5	1602.72522	±0.93524
w5	46.84244	±3.29177
A5	15.28175	±2.13612

Appendix figure 10:Peak fitting raman spectrum Ir (L11020D) position 2

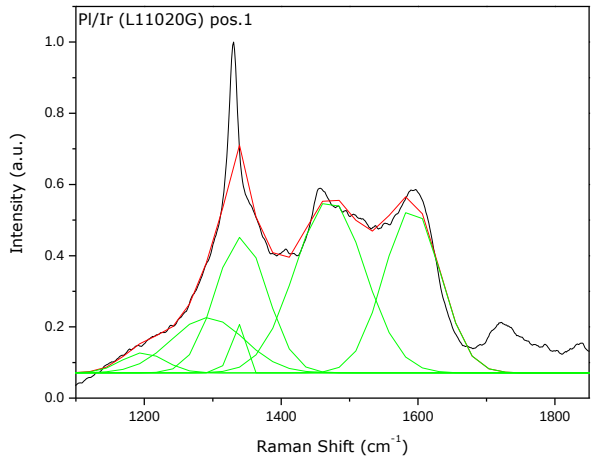

Data: G20_B
Model: Gauss
Equation: y=y0 + (A/(w*sqrt(PI/2)))*exp(-2*((x-xc)/w)^2)
Weighting:
y No weighting

Chi^2/DoF = 0.00214
R^2 = 0.94705

y0	0.07087	±0.00194
xc1	1198.35482	±50.01063
w1	63.13391	±68.14097
A1	4.47088	±21.39014
xc2	1293.02654	±644.13585
w2	105.67901	±547.39846
A2	20.57181	±291.70618
xc3	1329.7403	±0.37621
w3	12.28464	±0.94327
A3	6.44737	±0.65637
xc4	1341.55155	±25.73196
w4	75.37811	±75.94865
A4	36.06484	±268.68819
xc5	1471.12737	±9.96236
w5	101.40612	±24.40532
A5	61.76453	±19.88856
xc6	1591.54155	±4.21079
w6	82.07176	±4.62528
A6	47.54277	±5.65071

Appendix figure 11:Peak fitting raman spectrum Pl/Ir (L11020G) position 1

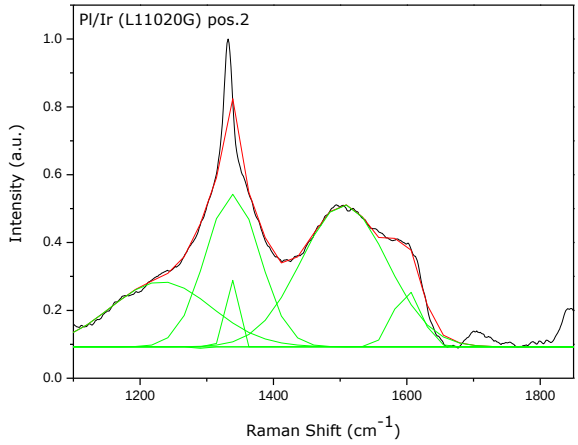

Data: G20_C
Model: Gauss
Equation: y=y0 + (A/(w*sqrt(PI/2)))*exp(-2*((x-xc)/w)^2)
Weighting:
y No weighting

Chi^2/DoF = 0.00174
R^2 = 0.94596

y0	0.09257	±0.00182
xc1	1231.75089	±15.77953
w1	151.41738	±19.40763
A1	36.36444	±6.8429
xc2	1289.07612	±33.26832
w2	12.86365	±82.28998
A2	-0.06796	±0.52852
xc3	1331.8356	±0.39384
w3	12.84462	±0.95244
A3	5.83066	±0.52564
xc4	1338.75095	±2.18605
w4	81.73548	±5.44288
A4	46.09575	±6.90131
xc5	1505.79026	±2.0699
w5	129.0177	±6.46175
A5	67.70365	±3.06085
xc6	1600.66503	±1.54629
w6	41.61934	±4.88241
A6	8.68528	±1.71887

Appendix figure 12:Peak fitting raman spectrum Pl/Ir (L11020G) position 2

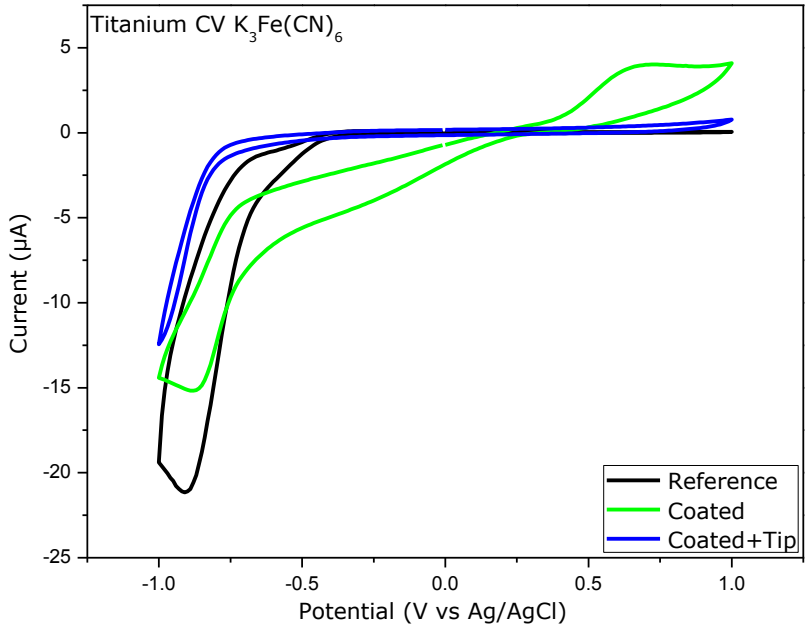

Appendix figure 13: Cyclic Voltammogram Ti electrode (L11018O) in $K_3Fe(CN)_6$

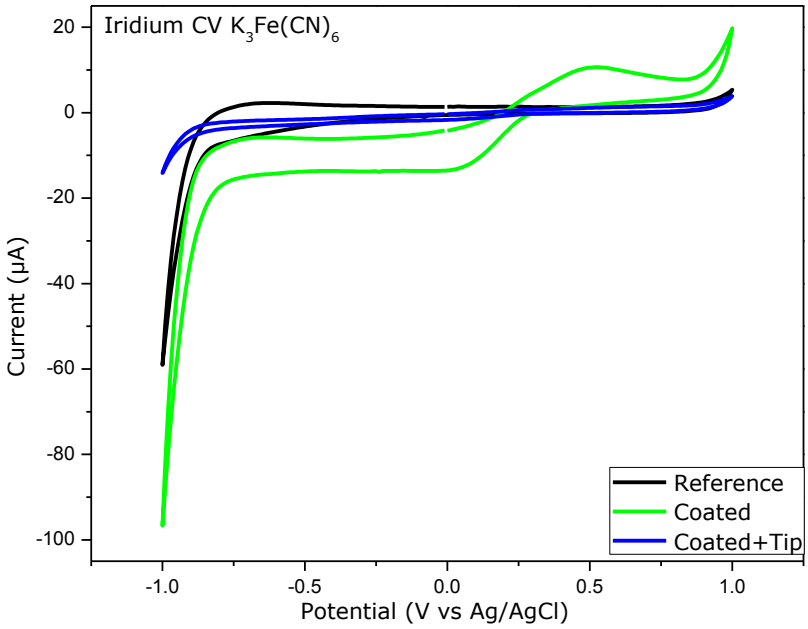

Appendix figure 14: Cyclic Voltammogram Ir electrode (L11020D) in $K_3Fe(CN)_6$

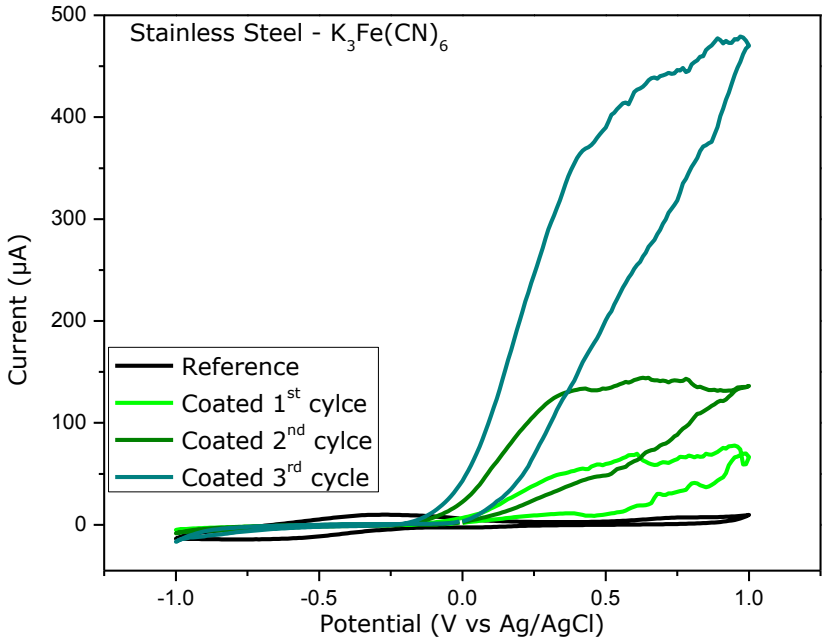

Appendix figure 15: Cyclic Voltrammogram SS electrode (L11018M) in $K_3Fe(CN)_6$

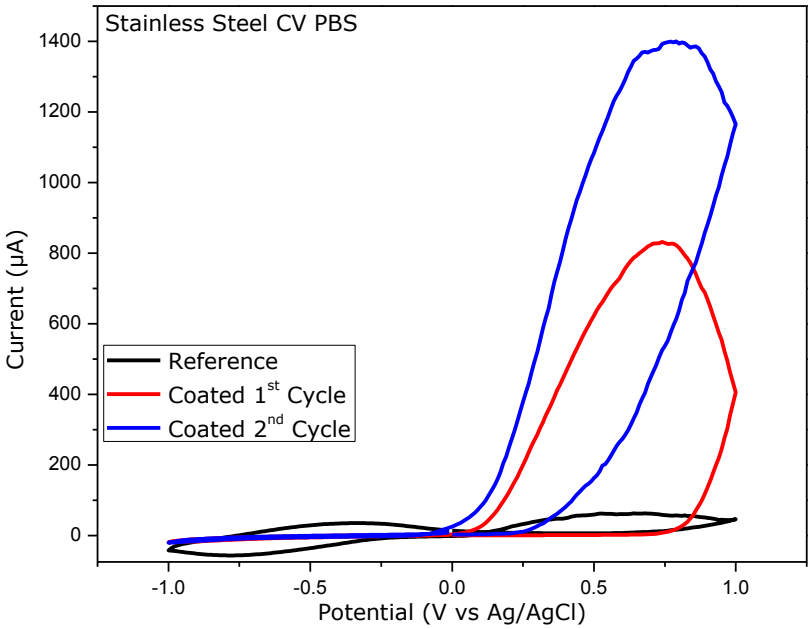

Appendix figure 16: Cyclic Voltrammogram SS electrode (L11018M) in PBS

Auteursrechtelijke overeenkomst

Ik/wij verlenen het wereldwijde auteursrecht voor de ingediende eindverhandeling:
Nanocrystalline Diamond Coating of Cardiac Stimulation Electrodes For Improved Biocompatibility: A Structural And Electrochemical Investigation

Richting: **master in de biomedische wetenschappen-bio-elektronica en nanotechnologie**
Jaar: **2011**

in alle mogelijke mediaformaten, - bestaande en in de toekomst te ontwikkelen - , aan de Universiteit Hasselt.

Niet tegenstaand deze toekenning van het auteursrecht aan de Universiteit Hasselt behoud ik als auteur het recht om de eindverhandeling, - in zijn geheel of gedeeltelijk -, vrij te reproduceren, (her)publiceren of distribueren zonder de toelating te moeten verkrijgen van de Universiteit Hasselt.

Ik bevestig dat de eindverhandeling mijn origineel werk is, en dat ik het recht heb om de rechten te verlenen die in deze overeenkomst worden beschreven. Ik verklaar tevens dat de eindverhandeling, naar mijn weten, het auteursrecht van anderen niet overtreedt.

Ik verklaar tevens dat ik voor het materiaal in de eindverhandeling dat beschermd wordt door het auteursrecht, de nodige toelatingen heb verkregen zodat ik deze ook aan de Universiteit Hasselt kan overdragen en dat dit duidelijk in de tekst en inhoud van de eindverhandeling werd genotificeerd.

Universiteit Hasselt zal mij als auteur(s) van de eindverhandeling identificeren en zal geen wijzigingen aanbrengen aan de eindverhandeling, uitgezonderd deze toegelaten door deze overeenkomst.

Voor akkoord,

Rendace, Romano

Datum: **22/08/2011**